Electronic Supplementary Information (ESI)

Effective modulation of the exotic properties of two-dimensional multifunctional TM_2@g-C_4N_3 monolayers via transition metal permutation and biaxial strain

De-Bing Long,[1] Yulin Feng,[2] Guoying Gao,[3] and Li-Ming Yang[1]*

[1]*Key Laboratory of Material Chemistry for Energy Conversion and Storage, Ministry of Education, Hubei Key Laboratory of Bioinorganic Chemistry and Materia Medica, Hubei Key Laboratory of Materials Chemistry and Service Failure, Hubei Engineering Research Center for Biomaterials and Medical Protective Materials, School of Chemistry and Chemical Engineering, Huazhong University of Science and Technology, Wuhan 430074, China. (email: Lmyang@hust.edu.cn)*
[2]*College of Physics and Electronic Science, Hubei Normal University, Huangshi 435002, China.*
[3]*School of Physics and Wuhan National High Magnetic Field Center, Huazhong University of Science and Technology, Wuhan 430074, China.*

Table of Contents:

(4) Magnetic properties

1. Spin densities of the remaining 10 magnetic TM_2@g-C_4N_3 monolayers: Fig. S13

2. Exchange energies E_{ex} ($E_{ex} = E_{AFM} - E_{FM}$, meV) and parameters ($J_i$, meV) per supercell, and Curie/Néel temperatures of 13 magnetic TM@g-C_4N_3 monolayers obtained from Monte Carlo simulations: Table S4

3. Schematic diagrams of three different magnetic ordering configurations in 2D g-C_4N_3 monolayer: Fig. S14

4. Comparison of collinear and non-collinear spin-polarized calculation results of pristine g-C_4N_3 and Re_2@g-C_4N_3 monolayers: Tables S5–S6

5. The calculated energy per transition metal atom along different magnetization orientations relative to the total energy with magnetization orientation parallel to easy axis (EA) and magnetic anisotropic energy (MAE) for TM_2@g-C_4N_3 monolayers: Table S7

6. Exchange energies and parameters per supercell, average magnetic moment per TM atom, and Curie/Néel temperatures under biaxial strains from –10% (–14%) to 10% for four representative materials: Table S8

7. Evolution of calculated Bader charges on TM atoms and g-C_4N_3 moiety of four representative materials versus biaxial strains from –10% (–14%) to 10%: Fig. S15

(5) Electronic properties

1. Calculated PBE+U and HSE06 band structures of the remaining 15 TM_2@g-C_4N_3 monolayers: Figs. S16–S17

2. Band gap values of TM_2@g-C_4N_3 monolayers calculated at PBE+U and HSE06 levels: Table S9

3. Charge density difference of the remaining 15 TM_2@g-C_4N_3 monolayers: Fig. S18

4. The evolution of PDOS of different atoms near the Fermi level versus biaxial strains from –10% (–14%) to 10% for four representative materials: Figs. S19–S22

(6) Optical properties

1. The evolution of optical absorption coefficient versus biaxial strains for Co_2@ and Zr_2@g-C_4N_3 monolayers: Figs. S23–S24

(1) Test of different U_{eff} values for magnetic ground states (MGS) and local magnetic moments *M* of TM atoms in TM_2@g-C_4N_3 monolayers

Table S1 The comparison of magnetic ground states (MGS) and local magnetic moments *M* (μ_B/TM) of TM atoms obtained at U_{eff} = 3 eV and other different U_{eff} values (2, 2.5, 3.5, 4 eV).

TM_2@g-C_4N_3	U_{eff} = 2		U_{eff} = 2.5		U_{eff} = 3		U_{eff} = 3.5		U_{eff} = 4	
	MGS	*M*	MGS	*M*	MGS	*M*	MGS	*M*	MGS	*M*
Sc	AFM2	0.23	AFM2	0.24	AFM2	0.26	AFM2	0.27	AFM2	0.29
V	AFM2	2.90	AFM2	2.92	AFM2	2.95	AFM2	2.96	AFM2	2.98
Mn	AFM2	4.64	AFM2	4.66	AFM2	4.69	AFM2	4.72	AFM2	4.74
Co	FM	1.79	FM	1.81	FM	1.84	FM	1.84	FM	1.85
Ni	AFM2	0.89	AFM2	0.90	AFM2	0.92	AFM2	0.93	AFM2	0.94
Zn	NM	0	NM	0	NM	0	NM	0	NM	0
Y	NM	0	NM	0	NM	0	NM	0	NM	0
Zr	FM	0.40	FM	0.41	FM	0.43	FM	0.43	FM	0.44
Ru	AFM1	2.45	AFM1	2.48	AFM1	2.54	AFM1	2.57	AFM1	2.61
Rh	AFM1	1.43	AFM1	1.47	AFM1	1.52	AFM1	1.56	AFM1	1.59
Pd	AFM2	0.66	AFM2	0.69	AFM2	0.71	AFM2	0.73	AFM2	0.75
Cd	NM	0	NM	0	NM	0	NM	0	NM	0
Lu	NM	0	NM	0	NM	0	NM	0	NM	0
Hf	NM	0	NM	0	NM	0	NM	0	NM	0
Re	AFM1	4.94	AFM1	4.97	AFM1	5.04	AFM1	5.08	AFM1	5.11
Os	AFM1	3.54	AFM1	3.56	AFM1	3.62	AFM1	3.67	AFM1	3.69
Ir	AFM1	1.30	AFM1	1.34	AFM1	1.38	AFM1	1.42	AFM1	1.46
Pt	AFM1	0.66	AFM1	0.68	AFM1	0.70	AFM1	0.72	AFM1	0.74

(2) Stepwise high-throughput screening together with viability analysis and stability evaluation for 210 candidates

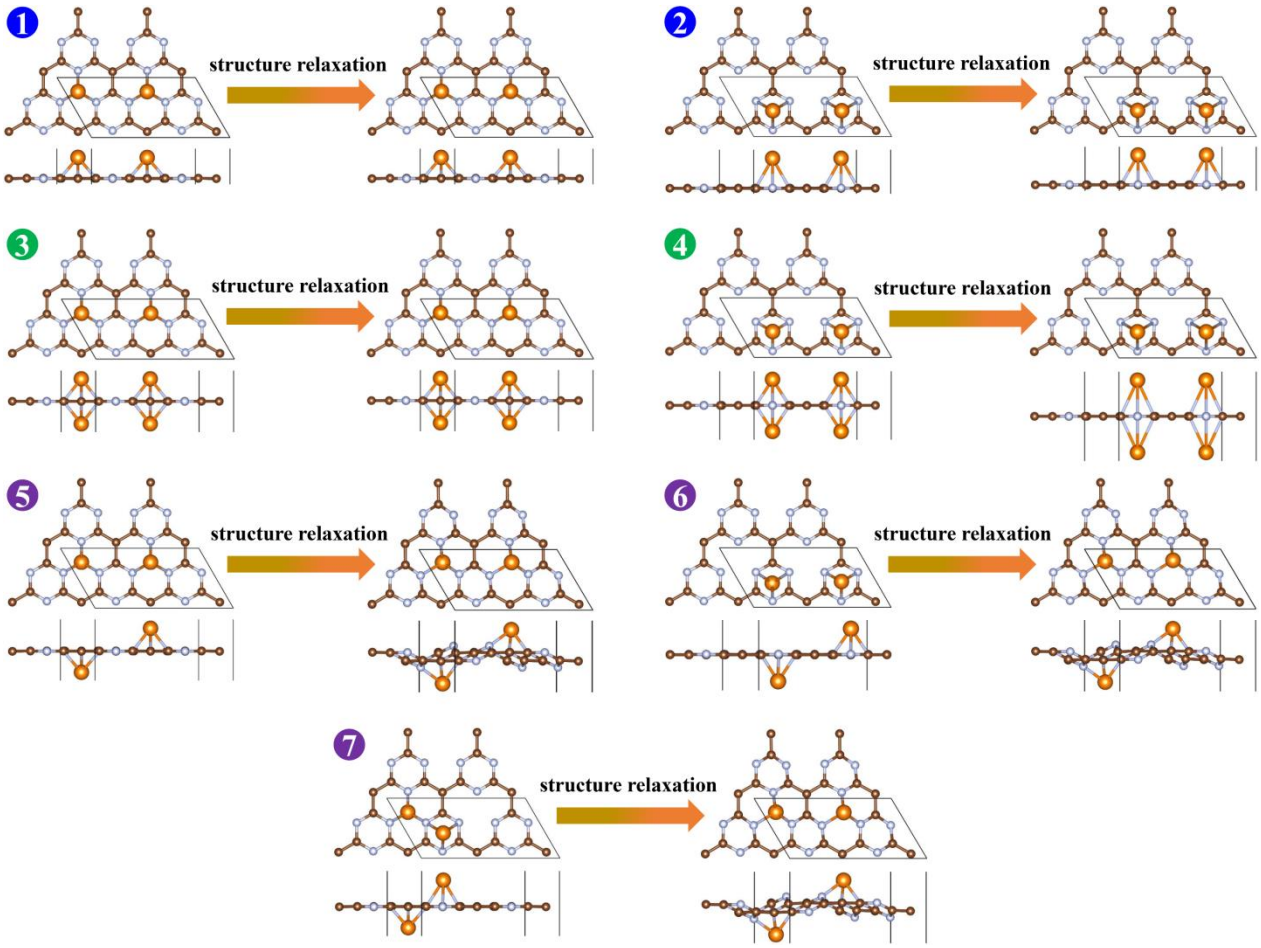

Fig. S1. Initial and final geometric structures before and after fully structural relaxation of the seven adsorption configurations.

Table S2 Calculated cohesive energies (E_c) of TM bulk and binding energies (E_b) of the TM atoms embedded in the g-C_4N_3 substrate in form of model-3 and model-5 as well as the calculated values of E_b + E_c. The experimental values of E_c are just for reference.

	E_c (eV/atom)		E_b (eV/atom)		E_b + E_c (eV/atom)	
TM	calc.	expt.[a)]	model-3	model-5	model-3	model-5
Sc	4.36	3.90	–3.41	–4.68	0.95	–0.31
Ti	5.50	4.90	–3.40	–4.68	2.09	0.81
V	5.40	5.30	–3.85	–5.45	1.55	–0.05
Cr	4.05	4.10	–2.04	–3.23	2.01	0.82
Mn	3.29	2.90	–2.24	–3.61	1.05	–0.32
Fe	4.63	4.30	–2.39	–3.86	2.24	0.77
Co	5.09	4.40	–2.83	–6.12	2.26	–1.02
Ni	4.74	4.40	–3.64	–5.30	1.11	–0.56
Cu	3.49	3.50	–2.10	–2.78	1.39	0.71
Zn	1.17	1.40	–0.53	–1.77	0.64	–0.60
Y	4.28	4.40	–4.59	–6.03	–0.31	–1.75
Zr	6.27	6.30	–4.60	–6.61	1.67	–0.34
Nb	7.02	7.60	–4.99	–5.18	2.04	1.84
Mo	6.36	6.80	–4.34	–5.76	2.02	0.60
Tc	7.07	6.90	–4.72	–7.01	2.36	0.06
Ru	7.03	6.70	–5.46	–7.76	1.57	–0.73
Rh	5.98	5.80	–3.41	–6.28	2.57	–0.30
Pd	3.74	3.90	–1.74	–3.83	2.01	–0.09
Ag	2.82	3.00	–1.33	–2.38	1.49	0.44
Cd	0.94	1.20	–0.42	–1.12	0.51	–0.19
Lu	4.32	4.43	–4.28	–6.00	0.04	–1.68
Hf	6.79	6.40	–4.76	–7.00	2.03	–0.21
Ta	8.47	8.10	–5.37	–7.43	3.11	1.04
W	8.49	8.90	–5.46	–7.30	3.03	1.19
Re	7.82	8.00	–4.96	–7.85	2.86	–0.04
Os	8.43	8.20	–5.40	–8.71	3.03	–0.28
Ir	7.56	6.90	–5.22	–7.77	2.35	–0.21
Pt	5.72	5.80	–2.77	–5.82	2.95	–0.10
Au	3.46	3.80	–1.31	–1.81	2.15	1.65
Hg	0.58	0.70	–0.34	–0.38	0.24	0.20

[a)] Kittel, C., Introduction to solid state physics. Wiley: 2005.

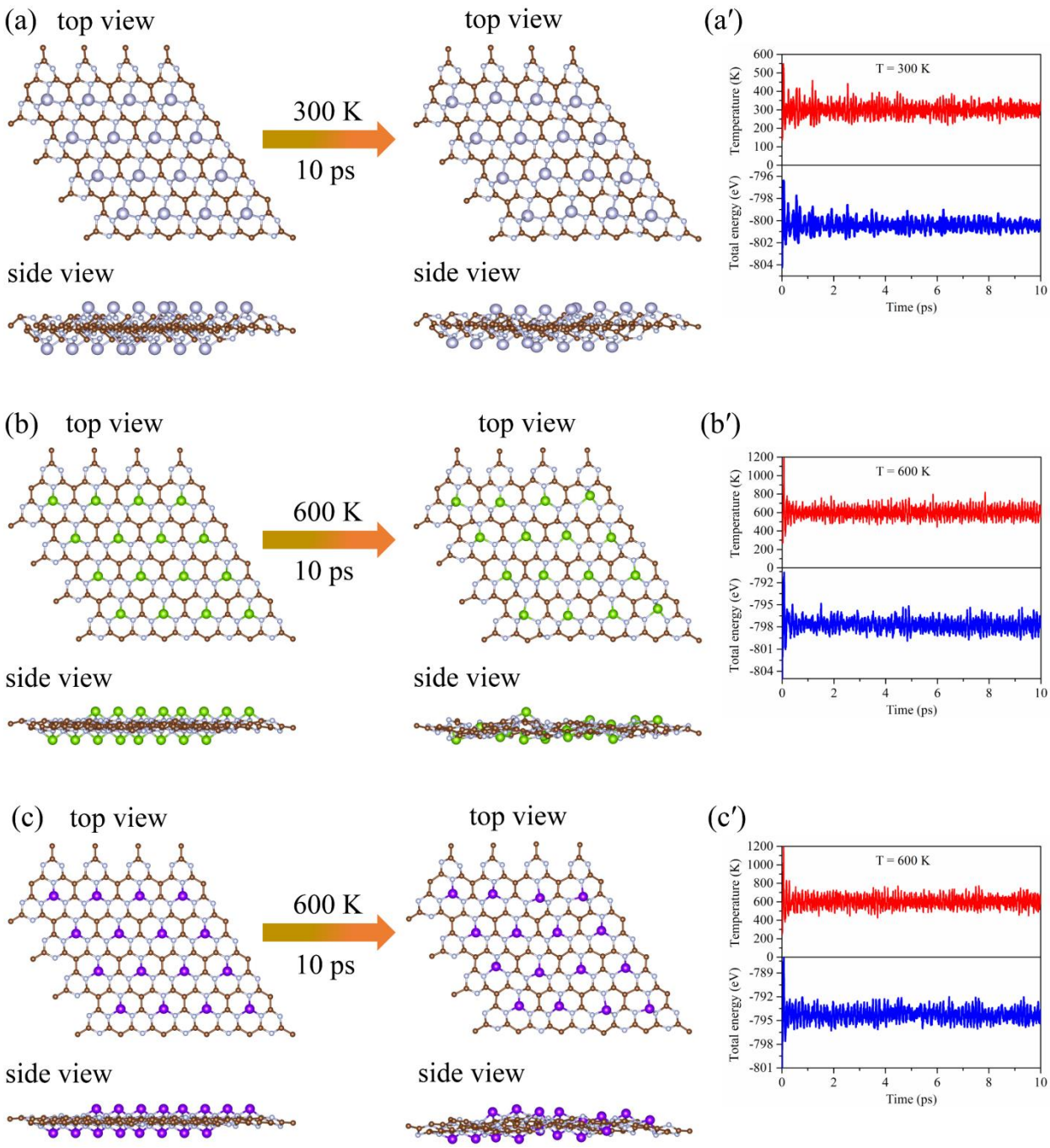

Fig. S2 Snapshots of the initial and final frames of AIMD simulations for asymmetrical adsorbed (a) Sc_2@, (b) V_2@, and (c) Mn_2@g-C_4N_3 monolayers at 300, 600, and 600 K, respectively. (a′)–(c′) are evolutions of the total energy and temperature versus the simulation time during AIMD simulations in (a)–(c).

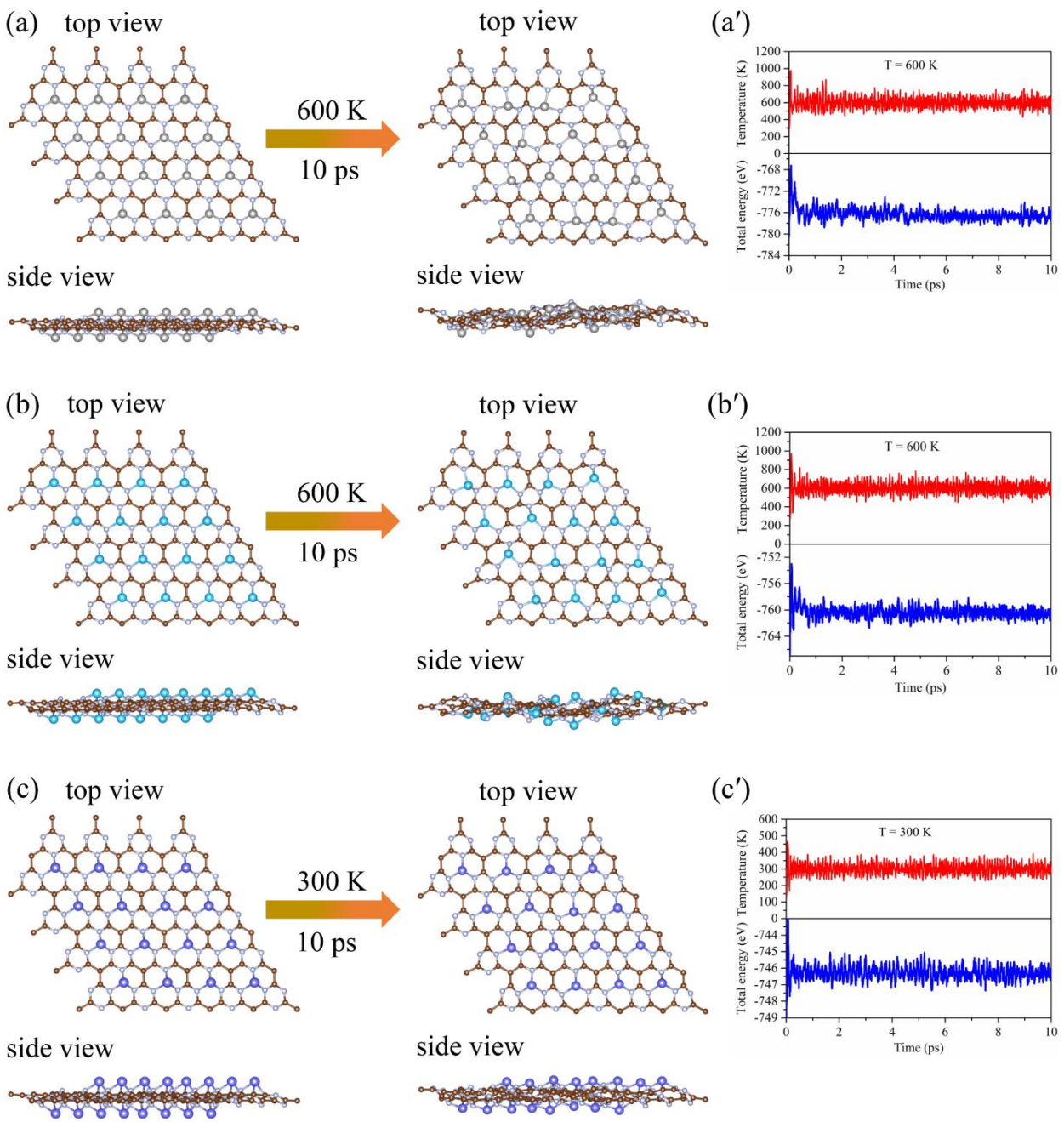

Fig. S3 Snapshots of the initial and final frames of AIMD simulations for asymmetrical adsorbed (a) Co_2@, (b) Ni_2@, and (c) Zn_2@g-C_4N_3 monolayers at 600, 600, and 300 K, respectively. (a′)–(c′) are evolutions of the total energy and temperature versus the simulation time during AIMD simulations in (a)–(c).

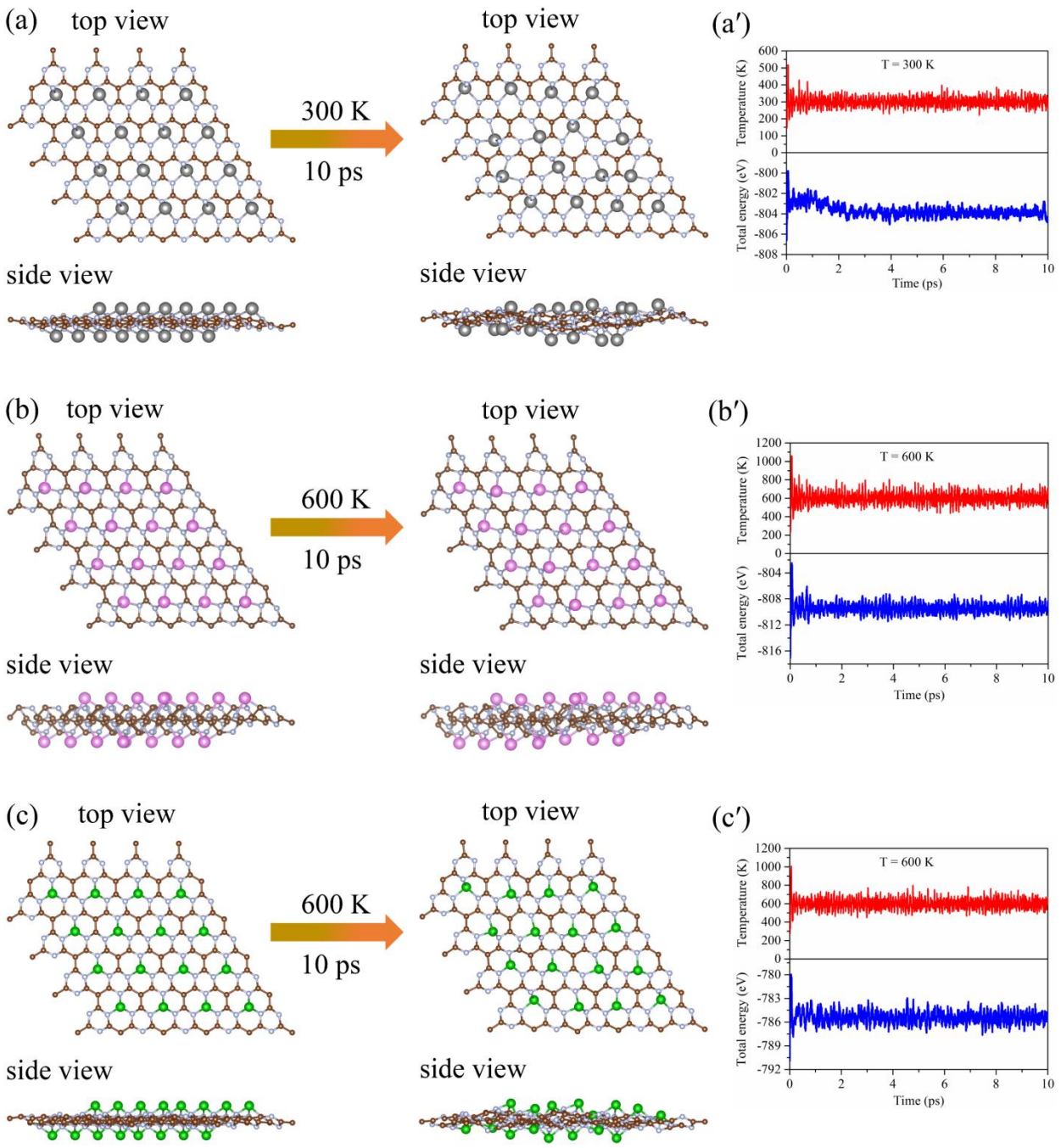

Fig. S4 Snapshots of the initial and final frames of AIMD simulations for asymmetrical adsorbed (a) Y_2@, (b) Zr_2@, and (c) Ru_2@g-C_4N_3 monolayers at 300, 600, and 600 K, respectively. (a′)–(c′) are evolutions of the total energy and temperature versus the simulation time during AIMD simulations in (a)–(c).

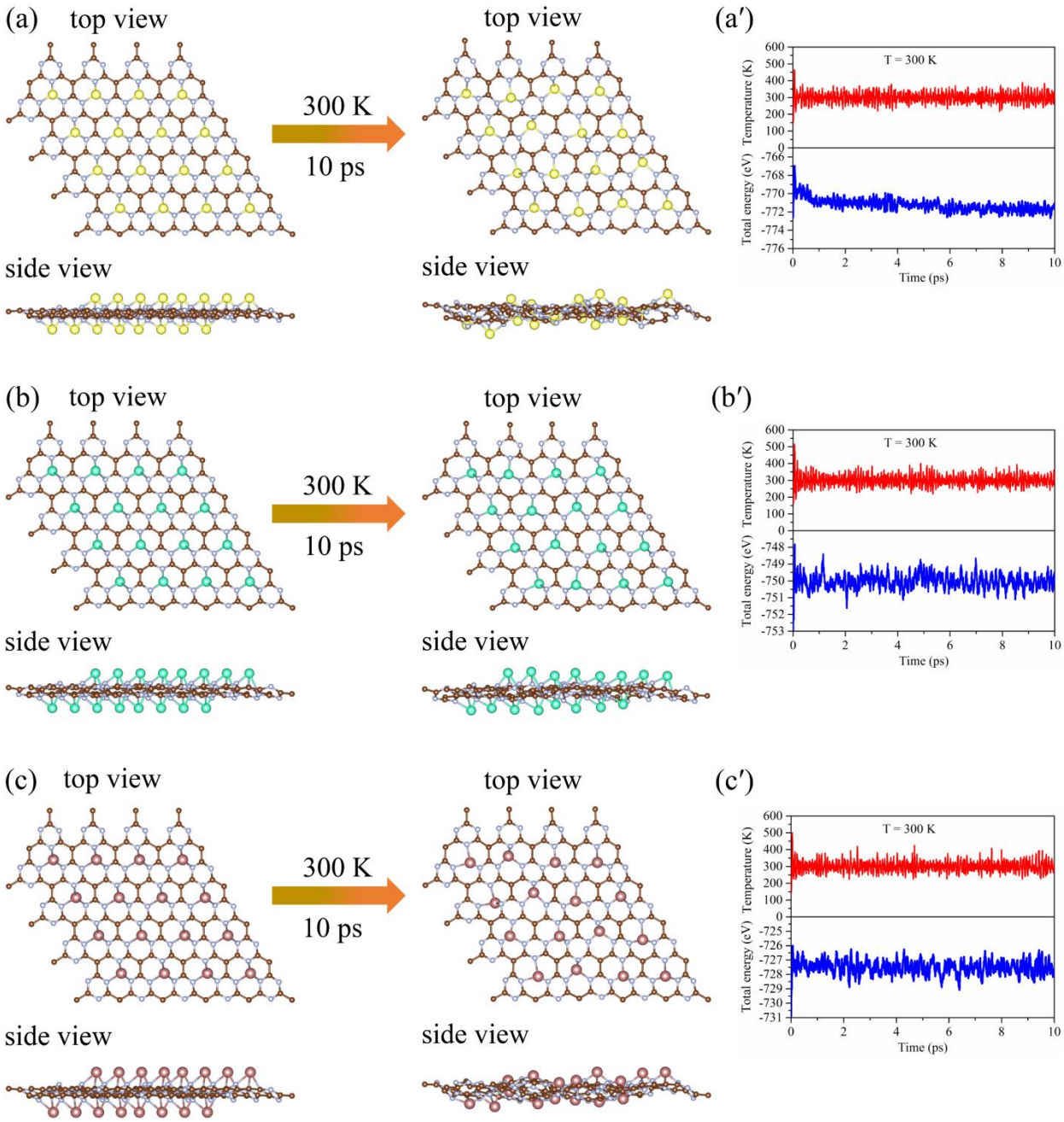

Fig. S5 Snapshots of the initial and final frames of AIMD simulations for asymmetrical adsorbed (a) Rh_2@, (b) Pd_2@, and (c) Cd_2@g-C_4N_3 monolayers at 300, 300, and 300 K, respectively. (a′)–(c′) are evolutions of the total energy and temperature versus the simulation time during AIMD simulations in (a)–(c).

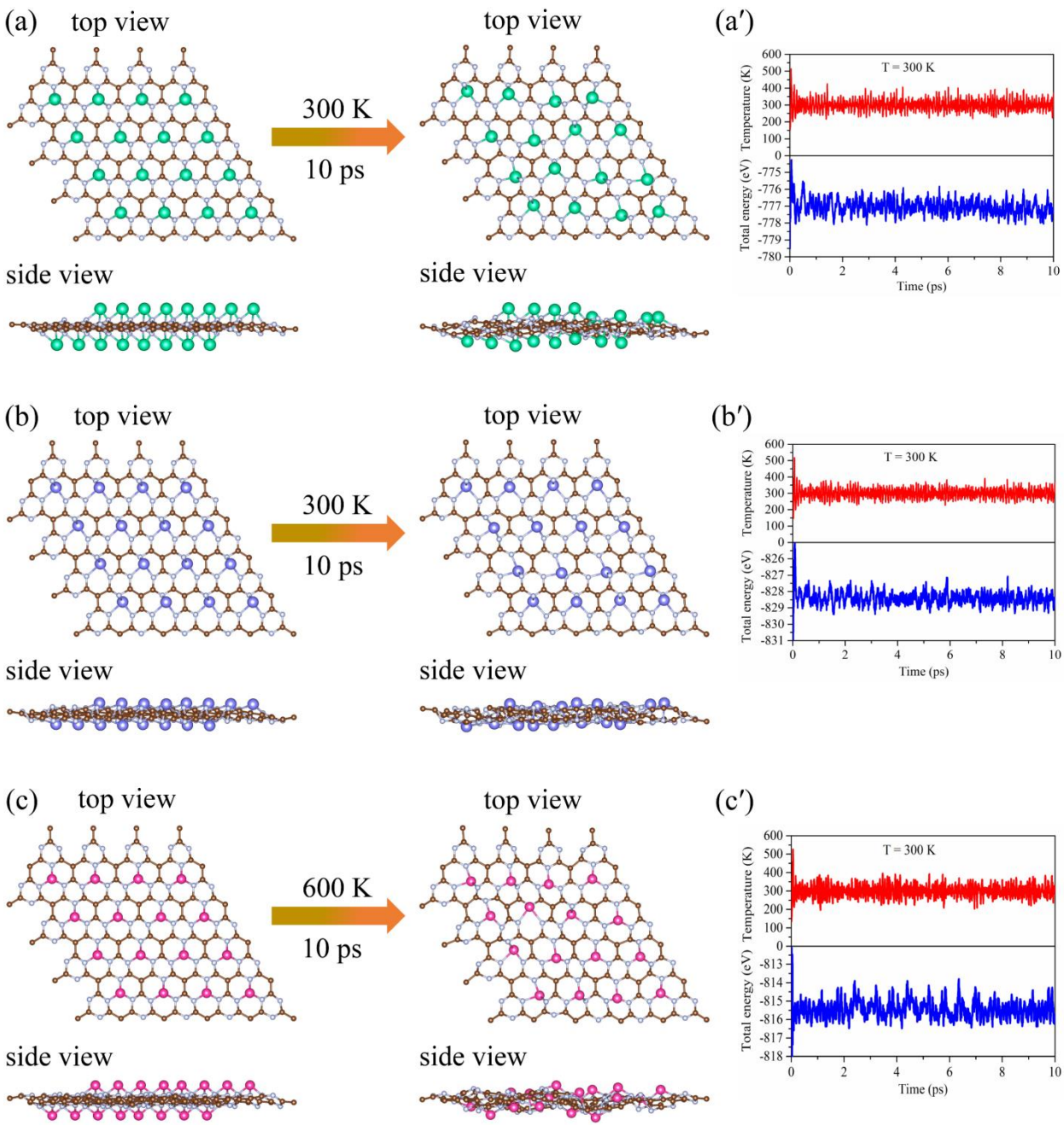

Fig. S6 Snapshots of the initial and final frames of AIMD simulations for asymmetrical adsorbed (a) Lu_2@, (b) Hf_2@, and (c) Re_2@g-C_4N_3 monolayers at 300, 300, and 600 K, respectively. (a′)–(c′) are evolutions of the total energy and temperature versus the simulation time during AIMD simulations in (a)–(c).

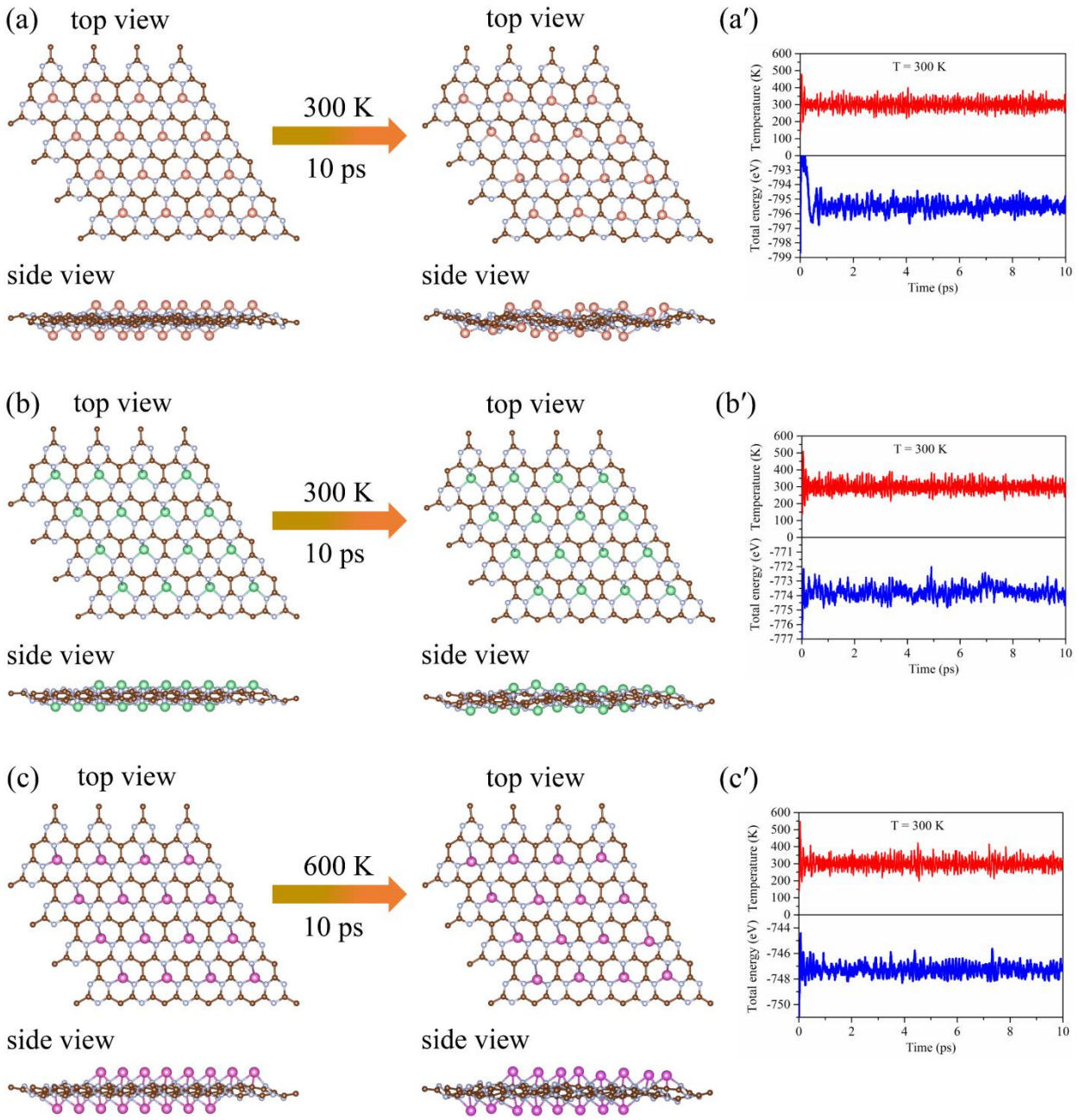

Fig. S7 Snapshots of the initial and final frames of AIMD simulations for asymmetrical adsorbed (a) Os_2@, (b) Ir_2@, and (c) Pt_2@g-C_4N_3 monolayers at 300, 300, and 600 K, respectively. (a′)–(c′) are evolutions of the total energy and temperature versus the simulation time during AIMD simulations in (a)–(c).

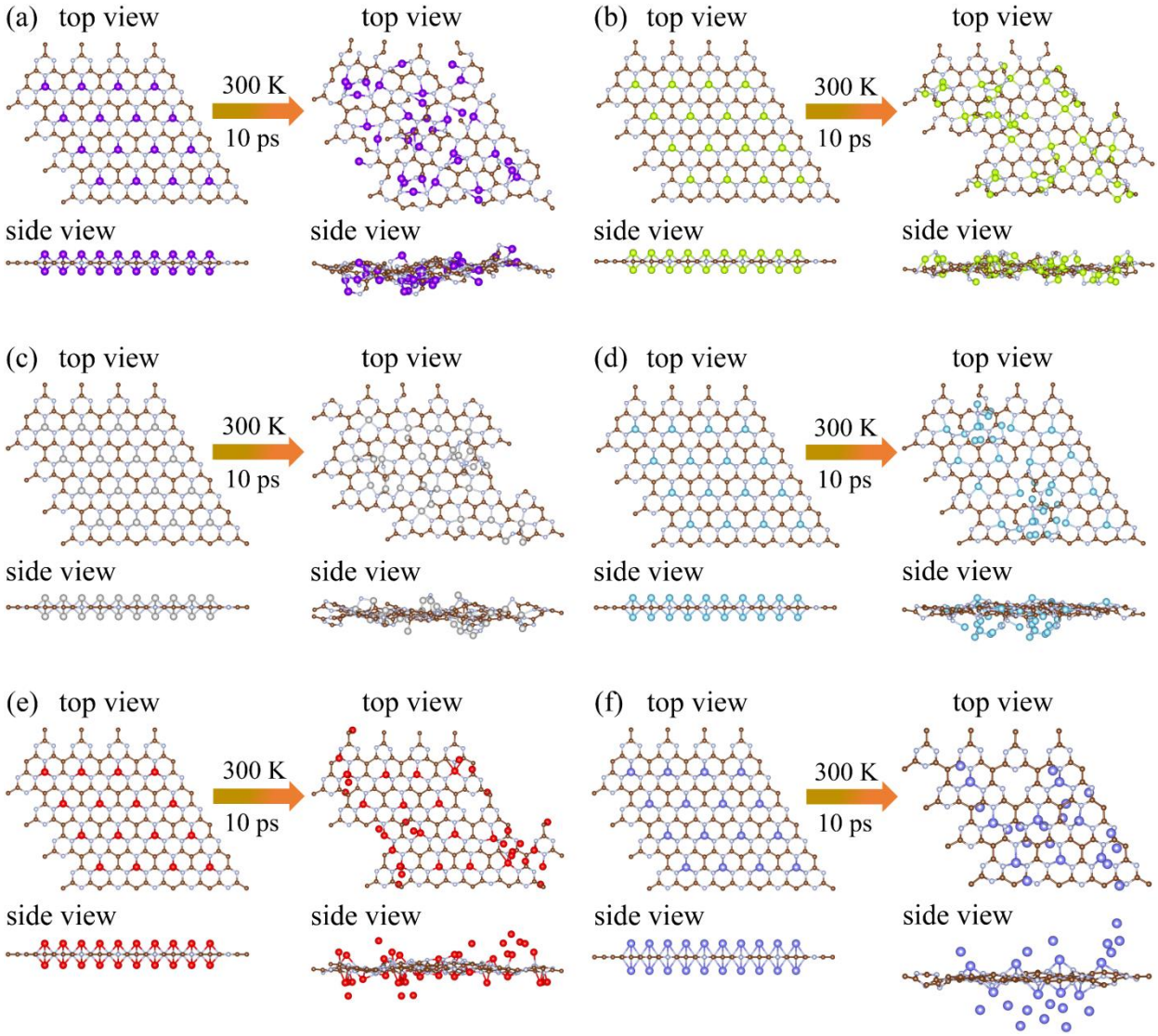

Fig. S8 Snapshots of the initial and final frames of AIMD simulations for symmetrical adsorbed (a) Mn_2@, (b) Fe_2@, (c) Co_2@, (d) Ni_2@, (e) Cu_2@, and (f) Zn_2@g-C_4N_3 monolayers at 300 K.

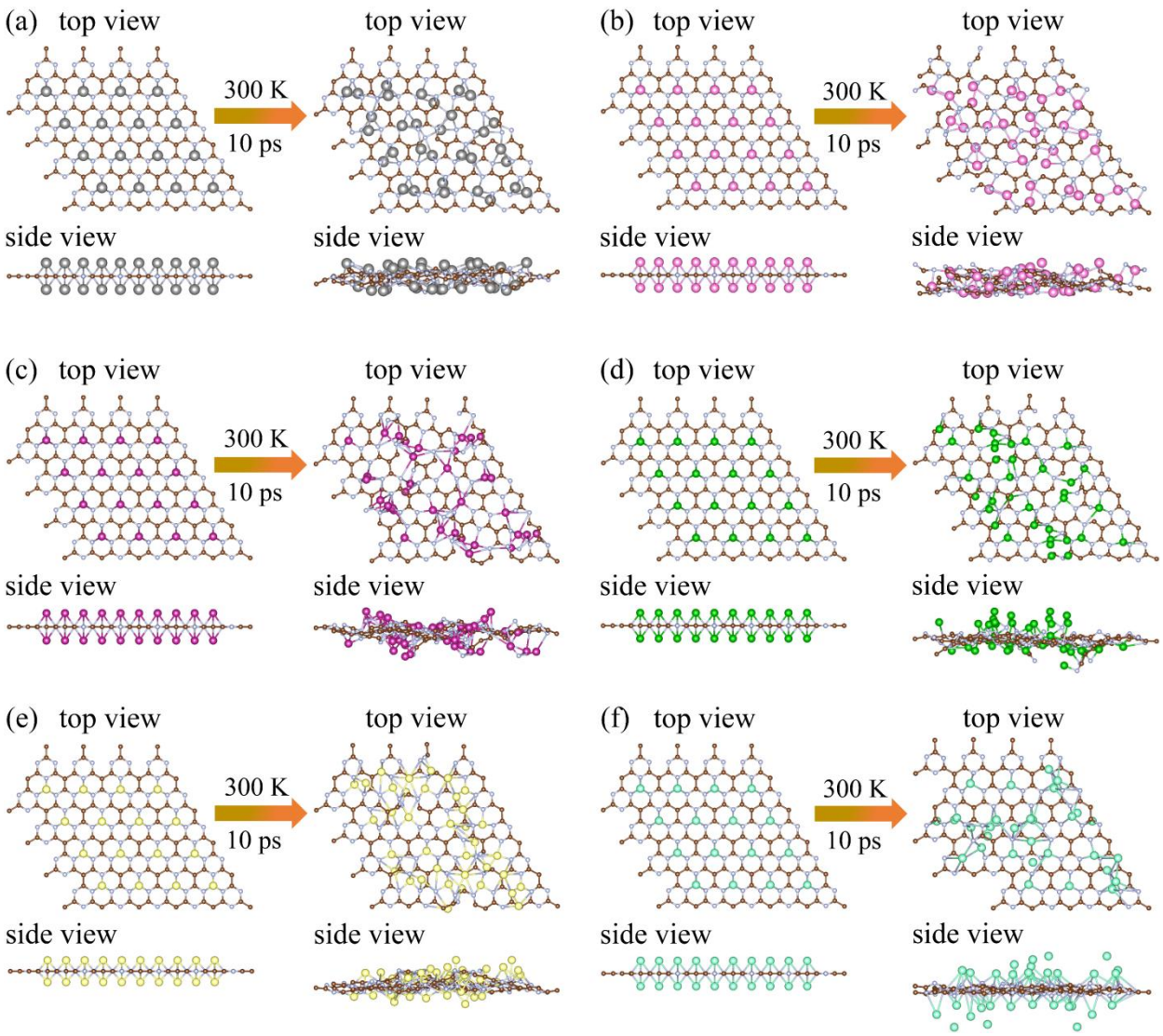

Fig. S9 Snapshots of the initial and final frames of AIMD simulations for symmetrical adsorbed (a) Y_2@, (b) Zr_2@, (c) Tc_2@, (d) Ru_2@, (e) Rh_2@, and (f) Pd_2@g-C_4N_3 monolayers at 300 K.

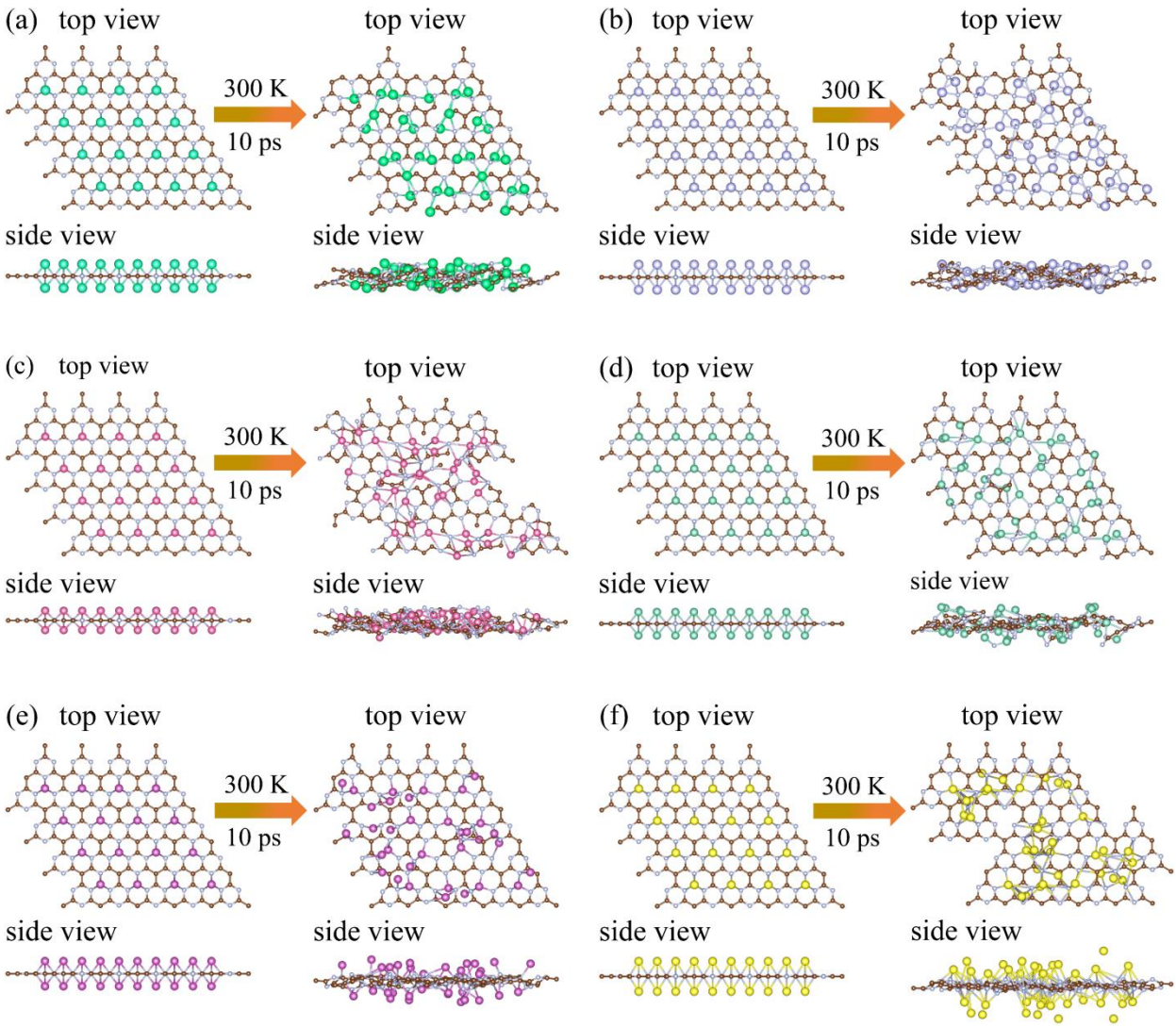

Fig. S10 Snapshots of the initial and final frames of AIMD simulations for symmetrical adsorbed (a) Lu_2@, (b) Hf_2@, (c) Re_2@, (d) Ir_2@, (e) Pt_2@, and (f) Au_2@g-C_4N_3 monolayers at 300 K.

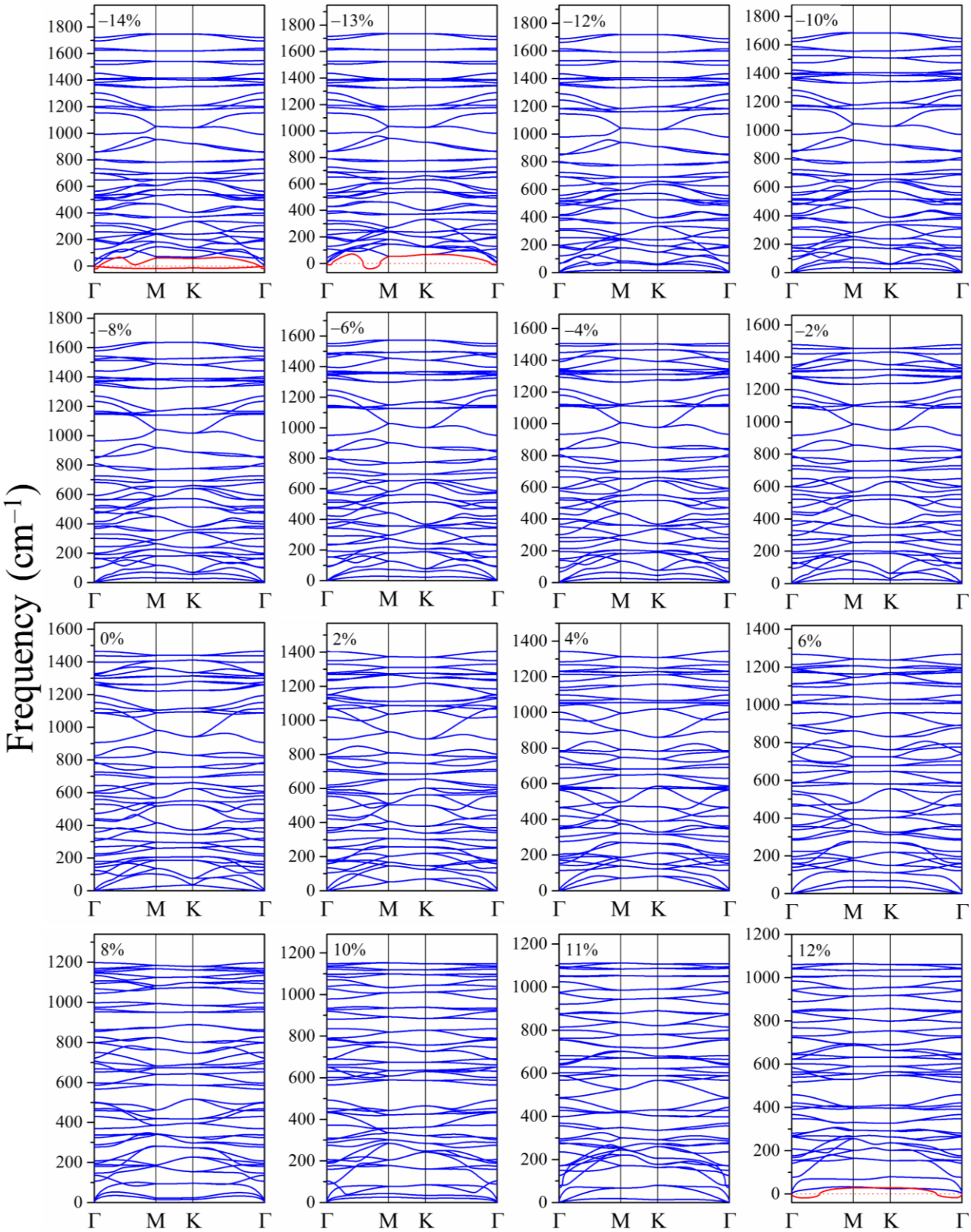

Fig. S11 Phonon dispersion spectra for Co_2@g-C_4N_3 monolayers under biaxial strains from –14% to 12%. The red color lines show the negative frequency (instability) at critical strains (–14%, –13% and 12%), the stable interval of strain of phonon spectra is –12% ~ 11%.

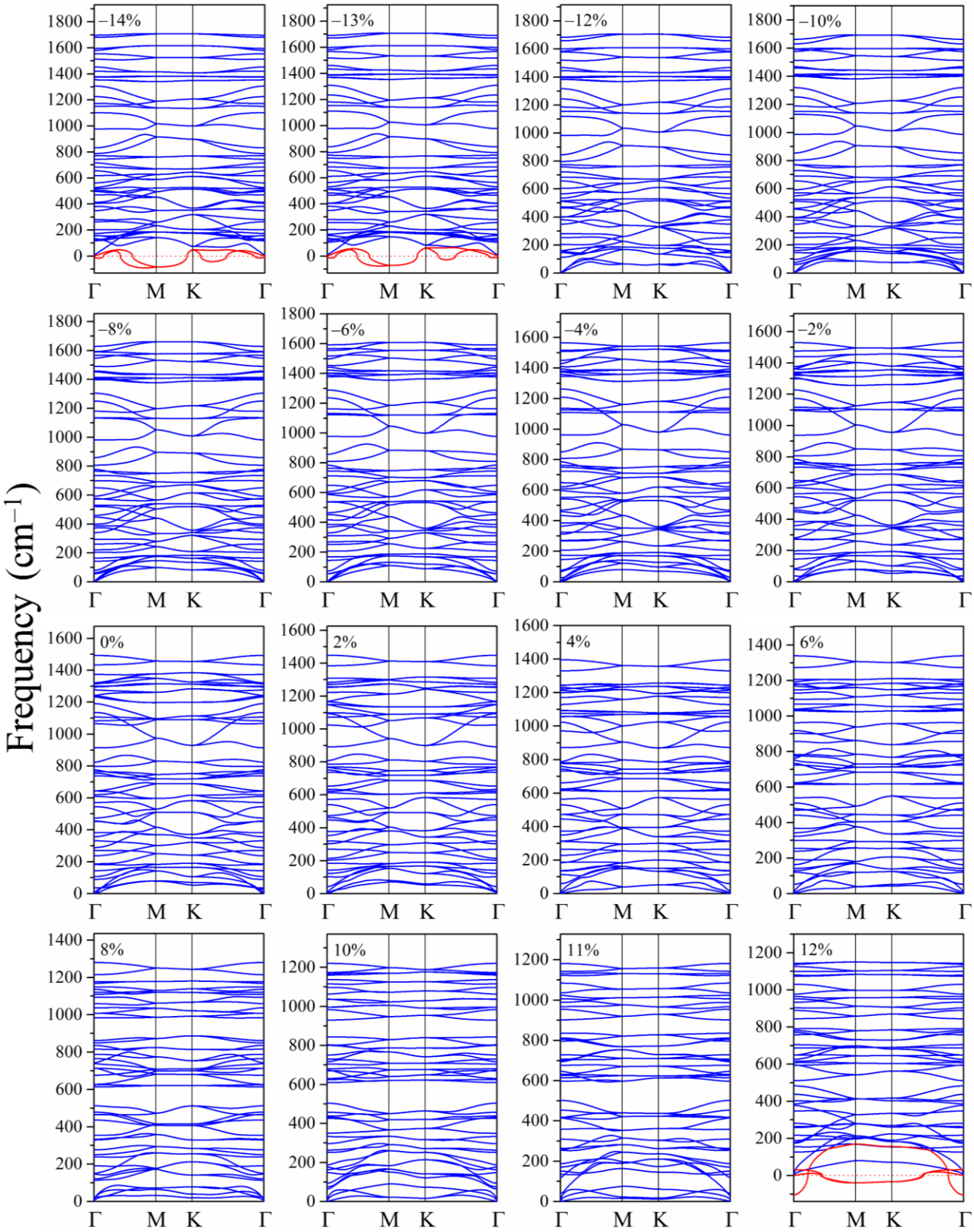

Fig. S12 Phonon dispersion spectra for Zr_2@g-C_4N_3 monolayers under biaxial strains from –14% to 12%. The red color lines show the negative frequency (instability) at critical strains (–14%, –13% and 12%), the stable interval of strain of phonon spectra is –12% ~ 11%.

(3) Crystal structure information of 18 stable TM_2@g-C_4N_3 monolayers

Table S3 The magnetic ground states (MGS), crystal structures, space groups, lattice parameters (Å), total magnetic moment per supercell (M_{tot}, μ_B), individual magnetic moment (M_{TM}, μ_B) of the TM atoms, and the distance between two TM atoms ($d_{TM\text{-}TM}$, Å) including nearest neighbor $d1$ and next-nearest neighbor $d2$, TM-N and C-N bond lengths ($R_{TM\text{-}N}$ and $R_{C\text{-}N}$, Å) for the optimized 18 TM_2@g-C_4N_3 monolayers in 2 × 2 × 1 supercells.

TM_2@g-C_4N_3	MGS	Crystal structure	Space group	Lattice parameters	M_{tot}	M_{TM}	$d_{TM\text{-}TM}$	$R_{TM\text{-}N}$	$R_{C\text{-}N}$
Sc_2@g-C_4N_3	AFM2	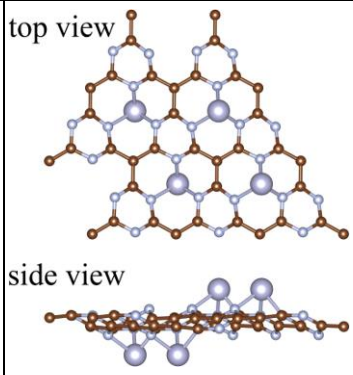	*P*3m1 (No. 156)	a = 9.70 b = 9.70 c = 15.51	0	Sc1: 0.26 Sc2: –0.26 Sc3: 0.26 Sc4: –0.26	*d*1: 4.87 *d*2: 6.13	2.10	1.34 1.39 1.40
V_2@g-C_4N_3	AFM2	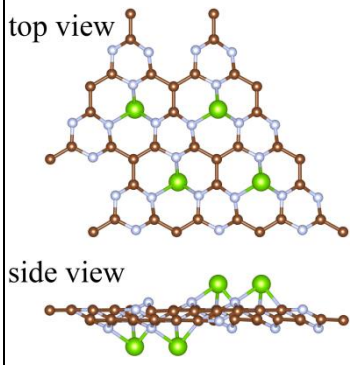	*P*3m1 (No. 156)	a = 9.70 b = 9.70 c = 15.54	0	V1: 2.95 V2: –2.95 V3: 2.95 V4: –2.95	*d*1: 4.89 *d*2: 6.02	2.06	1.34 1.37 1.39
Mn_2@g-C_4N_3	AFM2	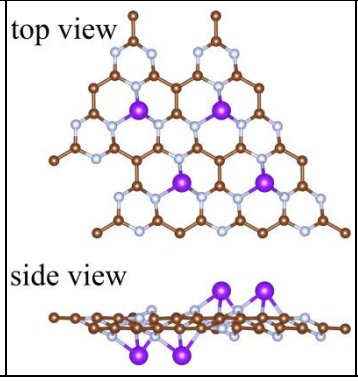	*P*3m1 (No. 156)	a = 9.69 b = 9.69 c = 15.59	0	Mn1: 4.69 Mn2: –4.69 Mn3: 4.69 Mn4: –4.69	*d*1: 4.90 *d*2: 6.10	2.12	1.34 1.37 1.38

Co_2@g-C_4N_3	FM	top view 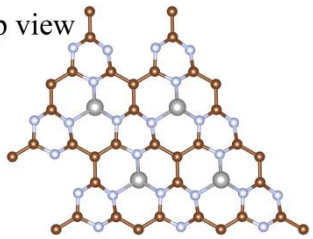 side view 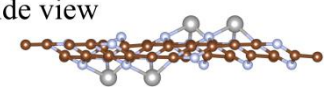	*P*3m1 (No. 156)	a = 9.73 b = 9.73 c = 15.54	8.00	Co1: 1.84 Co2: 1.84 Co3: 1.84 Co4: 1.84	*d*1: 4.93 *d*2: 5.71	1.90	1.35 1.37 1.38
Ni_2@g-C_4N_3	AFM2	top view 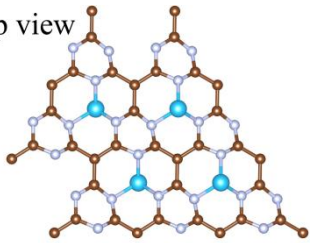 side view 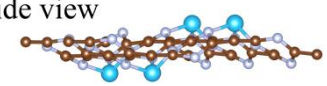	*P*3m1 (No. 156)	a = 9.65 b = 9.65 c = 15.62	0	Ni1: 0.92 Ni2: –0.92 Ni3: 0.92 Ni4: –0.92	*d*1: 4.90 *d*2: 5.52	1.86	1.34 1.35 1.38
Zn_2@g-C_4N_3	NM	top view 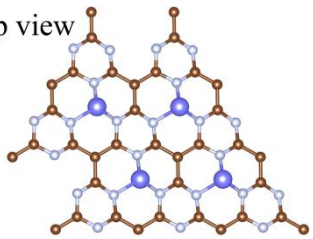 side view 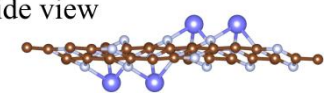	*P*3m1 (No. 156)	a = 9.71 b = 9.71 c = 15.53	0	0	*d*1: 4.91 *d*2: 5.89	2.02	1.35 1.36 1.37
Y_2@g-C_4N_3	NM	top view 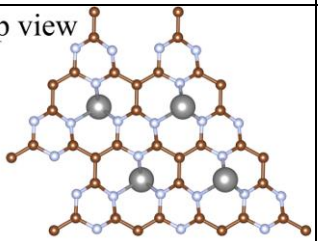 side view 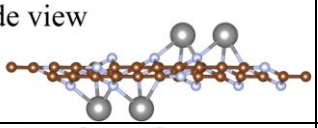	*P*3m1 (No. 156)	a = 9.68 b = 9.68 c = 15.55	0	0	*d*1: 4.85 *d*2: 6.42	2.30	1.34 1.38 1.39
Zr_2@g-C_4N_3	FM	top view 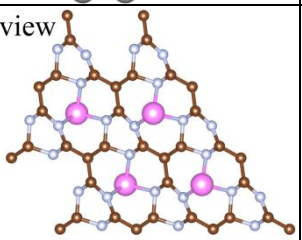 side view 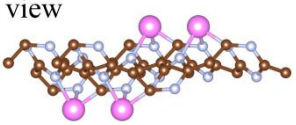	*P*3m1 (No. 156)	a = 9.05 b = 9.05 c = 18.66	4.00	Zr1: 0.58 Zr2: 0.27 Zr3: 0.58 Zr4: 0.27	*d*1: 4.80 *d*2: 6.28	2.05	1.35 1.38 1.46

Ru_2@g-C_4N_3	AFM1	top view 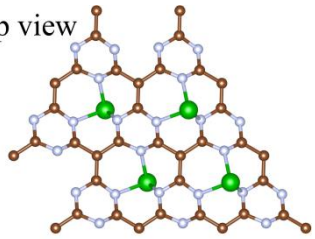 side view 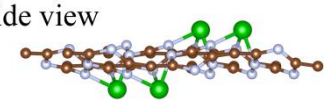	*P*3m1 (No. 156)	a = 9.56 b = 9.56 c = 15.92	0	Ru1: 2.54 Ru2: 2.54 Ru3: –2.54 Ru4: –2.54	*d*1: 4.79 *d*2: 5.86	2.15	1.35 1.37 1.40
Rh_2@g-C_4N_3	AFM1	top view 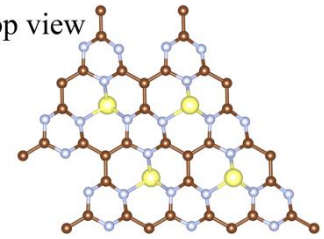 side view 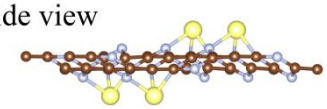	*P*3m1 (No. 156)	a = 9.67 b = 9.67 c = 15.71	0	Rh1: 1.52 Rh2: 1.52 Rh3: –1.52 Rh4: –1.52	*d*1: 4.90 *d*2: 6.11	2.11	1.34 1.36 1.38
Pd_2@g-C_4N_3	AFM2	top view 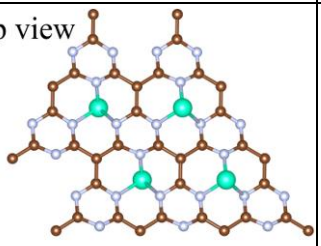 side view 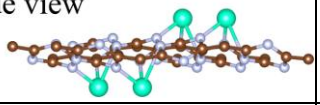	*P*3m1 (No. 156)	a = 9.59 b = 9.59 c = 16.00	0	Pd1: 0.71 Pd2: –0.71 Pd3: 0.71 Pd4: –0.71	*d*1: 4.80 *d*2: 6.19	2.09	1.34 1.35 1.38
Cd_2@g-C_4N_3	NM	top view 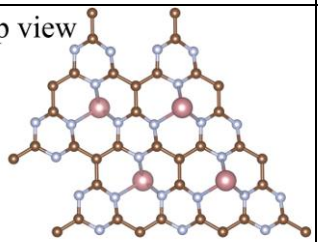 side view 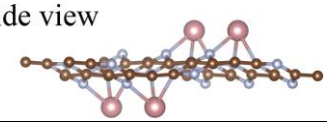	*P*3m1 (No. 156)	a = 9.64 b = 9.64 c = 15.76	0	0	*d*1: 4.88 *d*2: 6.48	2.36	1.34 1.36 1.37
Lu_2@g-C_4N_3	NM	top view 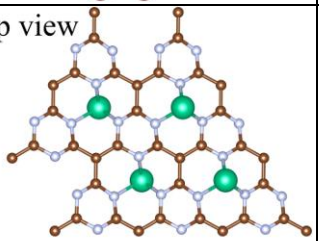 side view 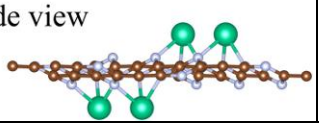	*P*3m1 (No. 156)	a = 9.67 b = 9.67 c = 15.59	0	0	*d*1: 4.86 *d*2: 6.42	2.30	1.34 1.37 1.38

Hf_2@g-C_4N_3	NM	top view 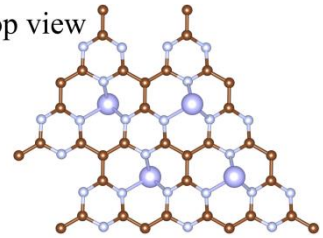 side view 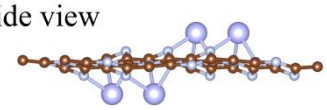	*P*3m1 (No. 156)	a = 9.72 b = 9.72 c = 15.38	0	0	*d*1: 4.86 *d*2: 6.01	2.15	1.34 1.38 1.40
Re_2@g-C_4N_3	AFM1	top view 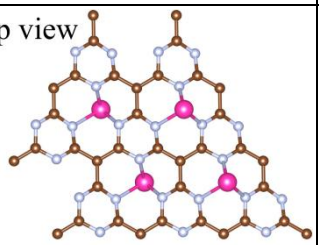 side view 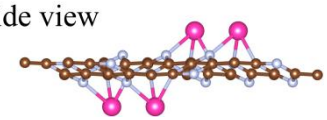	*P*3m1 (No. 156)	a = 9.65 b = 9.65 c = 15.71	0	Re1: 5.04 Re2: 5.04 Re3: –5.04 Re4: –5.04	*d*1: 4.88 *d*2: 6.48	2.33	1.35 1.36 1.37
Os_2@g-C_4N_3	AFM1	top view 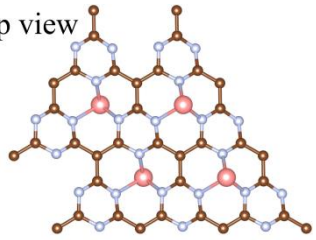 side view 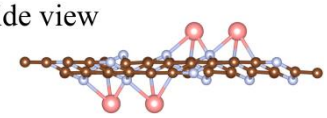	*P*3m1 (No. 156)	a = 9.67 b = 9.67 c = 15.67	0	Os1: 3.62 Os2: 3.62 Os3: –3.62 Os4: –3.62	*d*1: 4.88 *d*2: 6.36	2.30	1.35 1.36 1.37
Ir_2@g-C_4N_3	AFM1	top view 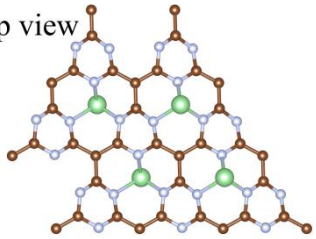 side view 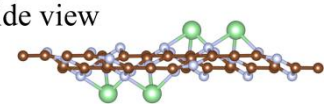	*P*3m1 (No. 156)	a = 9.68 b = 9.68 c = 15.69	0	Ir1: 1.38 Ir2: 1.38 Ir3: –1.38 Ir4: –1.38	*d*1: 4.88 *d*2: 6.02	2.10	1.35 1.36 1.38
Pt_2@g-C_4N_3	AFM2	top view 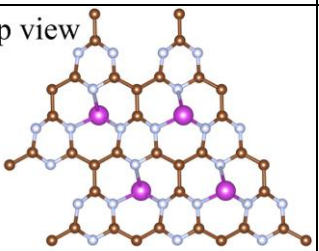 side view 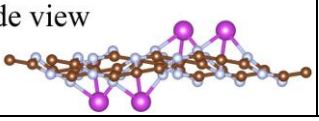	*P*3m1 (No. 156)	a = 9.47 b = 9.47 c = 16.07	0	Pt1: 0.70 Pt2: –0.70 Pt3: 0.70 Pt4: –0.70	*d*1: 4.79 *d*2: 6.13	2.06	1.33 1.35 1.39

(4) Magnetic properties

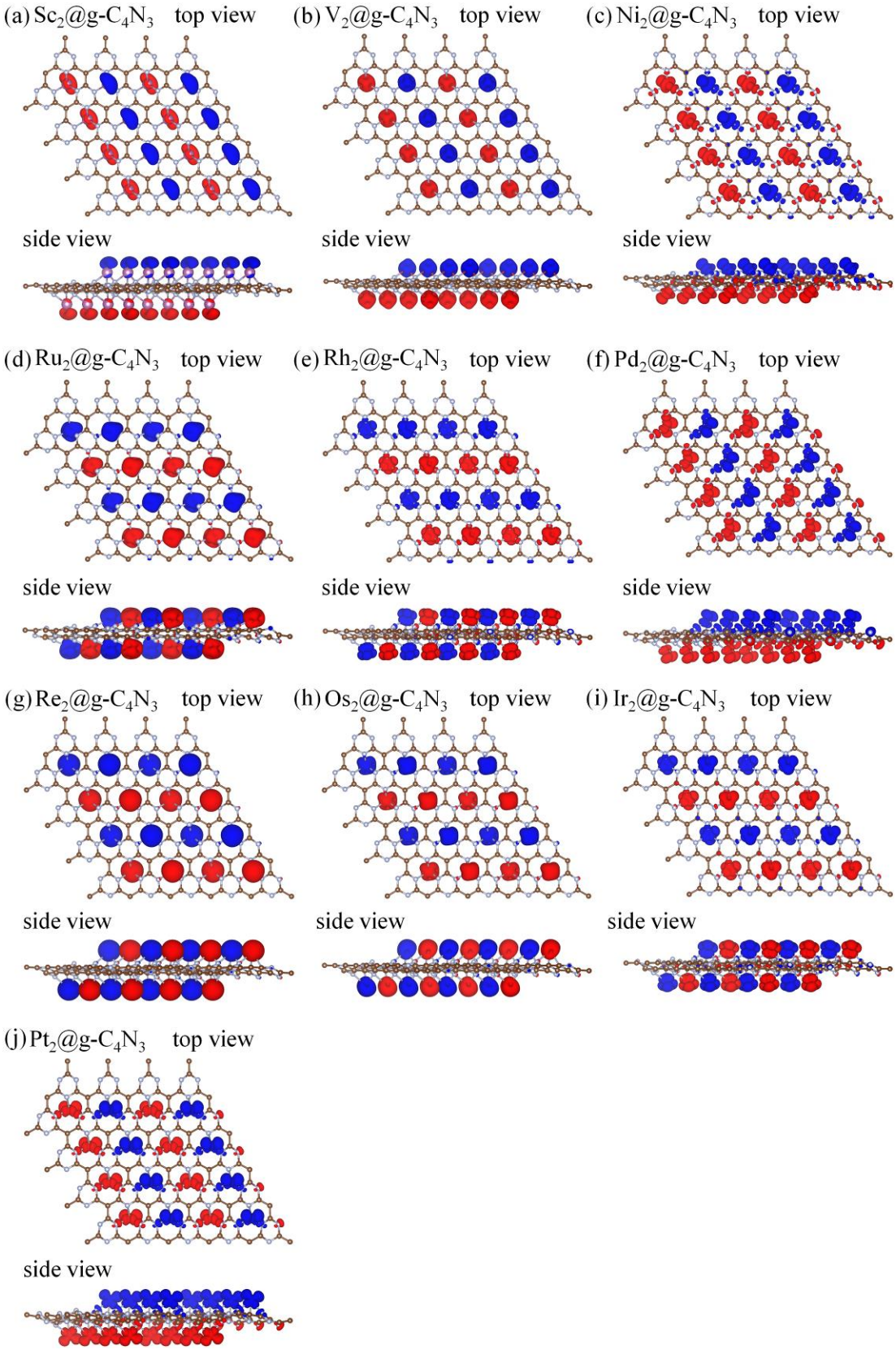

Fig. S13 Top and side views of the spin densities ($\Delta\rho = \rho_{\uparrow} - \rho_{\downarrow}$) for 2D periodic (a) Sc_2@, (b) V_2@, (c) Ni_2@, (d) Ru_2@, (e) Rh_2@, (f) Pd_2@, (g) Re_2@, (h) Os_2@, (i) Ir_2@, and (j) Pt_2@g-C_4N_3 monolayers in $2 \times 2 \times 1$ supercells at an isosurface value of 0.03 e $Å^{-3}$.

Table S4 Exchange energies E_{ex} ($E_{ex} = E_{AFM} - E_{FM}$, meV) and parameters ($J_i$, meV) per supercell, and Curie/Néel temperatures (T_C/T_N, K) of pristine g-C_4N_3 monolayer and 13 magnetic TM_2@g-C_4N_3 monolayers obtained from Monte Carlo (MC) simulations.

Structures	$E_{AFM1} - E_{FM}$	$E_{AFM2} - E_{FM}$	J_1	J_2	T_C/T_N
g-C_4N_3	741.940	770.760	685.974	660.324	295
Sc_2@g-C_4N_3	112.310	–13.430	245.854	–13.870	9.5
V_2@g-C_4N_3	158.630	–35.620	2.482	–0.251	13
Mn_2@g-C_4N_3	–11.360	–67.920	0.128	–0.193	49
Co_2@g-C_4N_3	8.110	46.090	–0.561	0.866	8.5
Ni_2@g-C_4N_3	–1.480	–1.720	–0.092	–0.128	< 5
Zr_2@g-C_4N_3	99.260	24.240	60.589	8.427	41.5
Ru_2@g-C_4N_3	–378.330	–41.320	–6.838	–0.395	< 5
Rh_2@g-C_4N_3	–126.030	–31.580	–5.562	–0.797	< 5
Pd_2@g-C_4N_3	–57.860	–59.600	–6.673	–7.087	24
Re_2@g-C_4N_3	–225.380	–101.080	–0.841	–0.243	< 5
Os_2@g-C_4N_3	–229.710	–137.640	–1.484	–0.635	< 5
Ir_2@g-C_4N_3	–51.290	–4.640	–2.920	–0.138	< 5
Pt_2@g-C_4N_3	–0.860	–55.260	6.314	–6.517	22.5

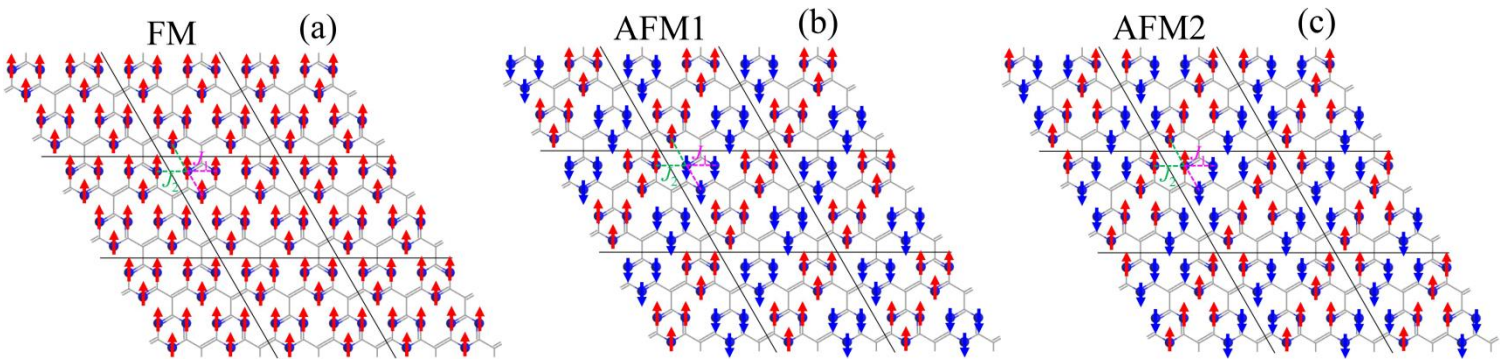

Fig. S14 Schematic diagrams for different magnetic ordering configurations in 2D g-C_4N_3 monolayer. (a) ferromagnetic (FM), (b) antiferromagnetic-1 (AFM1), and (c) antiferromagnetic-2 (AFM2). Blue balls are N atoms, and the arrows indicate the spin directions of the N atoms. The nearest (J_1) and second-nearest (J_2) exchange interactions are indicated by magenta and green dotted lines, respectively.

$$E(\mathrm{FM}) = E_0 - 12J_1M^2 - 12J_2M^2 \tag{1}$$

$$E(\mathrm{AFM1}) = E_0 - 12J_1M^2 + 4J_2M^2 \tag{2}$$

$$E(\mathrm{AFM2}) = E_0 + 4J_1M^2 - 12J_2M^2 \tag{3}$$

$$J_1 = \frac{E(\mathrm{AFM2}) - E(\mathrm{FM})}{16M^2} \tag{4}$$

$$J_2 = \frac{E(\mathrm{AFM1}) - E(\mathrm{FM})}{16M^2} \tag{5}$$

Table S5 Comparison of collinear and non-collinear spin-polarized calculation results of pristine g-C_4N_3 monolayer.

Collinear spin-polarized calculation					
Magnetic configuration	Before optimization	After optimization	Magnetic moments (μ_B)	Total energies (eV)	Relative energy (eV)
FM	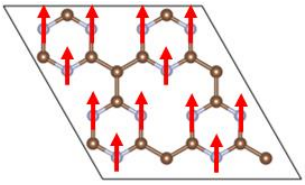	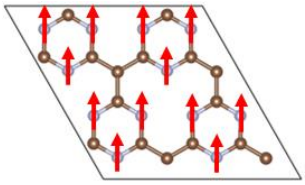	N1: 0.265 N2: 0.265 N3: 0.254 N4: 0.254 N5: 0.276 N6: 0.276 N7: 0.265 N8: 0.265 N9: 0.254 N10: 0.254 N11: 0.276 N12: 0.276	–236.04093	0
AFM1	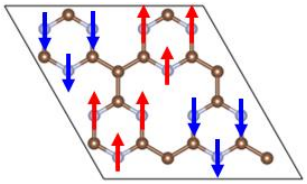	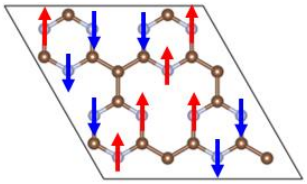	N1: 0.171 N2: –0.171 N3: 0.141 N4: –0.141 N5: –0.026 N6: 0.026 N7: –0.171 N8: 0.171 N9: –0.141 N10: 0.141 N11: 0.026 N12: –0.026	–235.75519	0.286
AFM2	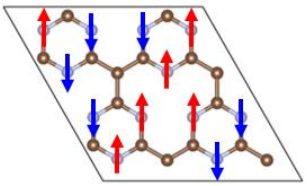	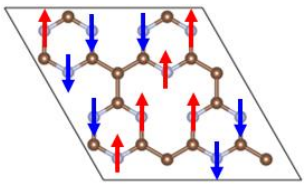	N1: 0.156 N2: –0.156 N3: 0.156 N4: –0.156 N5: –0.027 N6: 0.027 N7: –0.156 N8: 0.156 N9: –0.156 N10: 0.156 N11: 0.027 N12: –0.027	–235.75534	0.286
Non-collinear spin-polarized calculation					
Magnetic configuration	Before optimization	After optimization	Magnetic moments (μ_B)	Total energies (eV)	Relative energy (eV)

FM	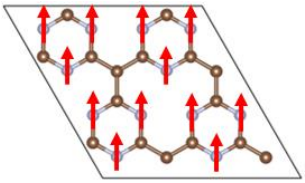	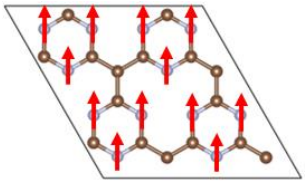	N1: 0.265 N2: 0.265 N3: 0.265 N4: 0.265 N5: 0.265 N6: 0.265 N7: 0.265 N8: 0.265 N9: 0.265 N10: 0.265 N11: 0.265 N12: 0.265	–236.04339	0
AFM1	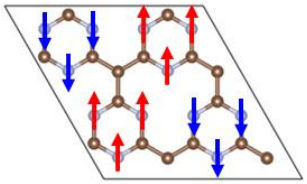	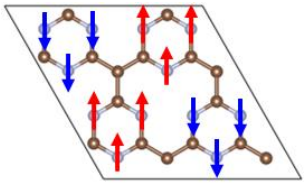	N1: 0.174 N2: –0.174 N3: 0.231 N4: –0.231 N5: 0.231 N6: –0.231 N7: 0.174 N8: –0.174 N9: 0.231 N10: –0.231 N11: 0.231 N12: –0.231	–235.30145	0.742
AFM2	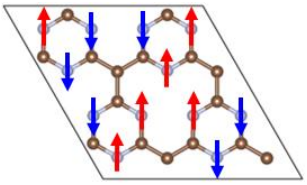	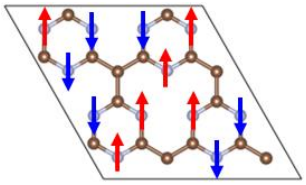	N1: 0.214 N2: –0.214 N3: 0.214 N4: –0.214 N5: –0.136 N6: 0.136 N7: –0.214 N8: 0.214 N9: –0.214 N10: 0.214 N11: 0.136 N12: –0.136	–235.27263	0.771

Table S6 Comparison of collinear and non-collinear spin-polarized calculation results of Re_2@g-C_4N_3 monolayer.

Collinear spin-polarized calculation					
Magnetic configuration	Before optimization	After optimization	Magnetic moments (μ_B)	Total energies (eV)	Relative energy (eV)
FM	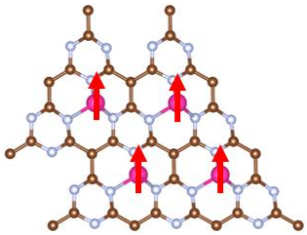	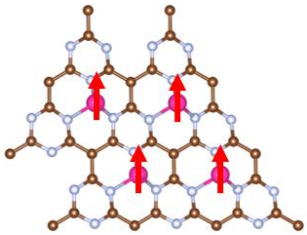	Re1: 5.098 Re2: 5.098 Re3: 5.098 Re4: 5.098	–262.20838	0
AFM1	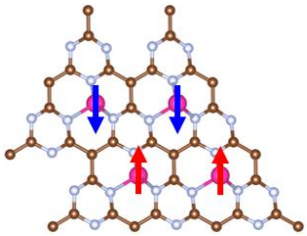	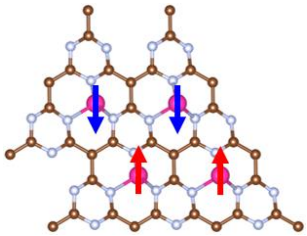	Re1: 5.036 Re2: 5.036 Re3: –5.036 Re4: –5.036	–262.43376	–0.225
AFM2	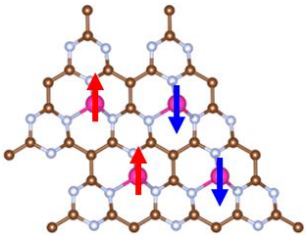	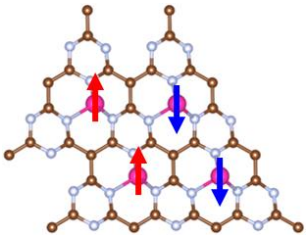	Re1: 5.055 Re2: –5.055 Re3: 5.055 Re4: –5.055	–262.30946	–0.101
Non-collinear spin-polarized calculation					
Magnetic configuration	Before optimization	After optimization	Magnetic moments (μ_B)	Total energies (eV)	Relative energy (eV)
FM	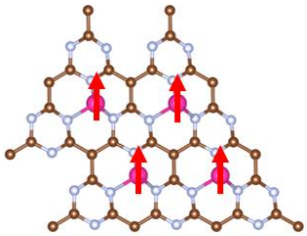	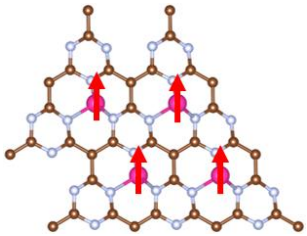	Re1: 5.095 Re2: 5.093 Re3: 5.097 Re4: 5.097	–262.21156	0
AFM1	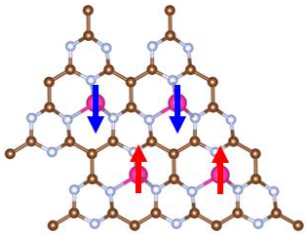	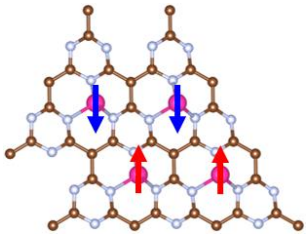	Re1: 5.037 Re2: 5.037 Re3: –5.036 Re4: –5.036	–262.43584	–0.224
AFM2	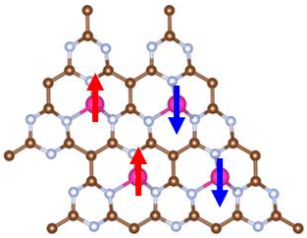	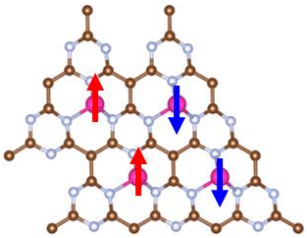	Re1: 5.055 Re2: –5.055 Re3: 5.055 Re4: –5.055	–262.31205	–0.101

Table S7 The calculated energy per transition metal atom (μeV/TM) along different magnetization orientations relative to the total energy with magnetization orientation parallel to easy axis (EA) and magnetic anisotropic energy (MAE, μeV/TM) are summarized for TM_2@g-C_4N_3 monolayers. The relative energy of EA was set to be 0.

TM_2@g-C_4N_3	E[100]	E[010]	E[110]	E[001]	E[111]	EA	MAE
Sc	18	100	35	0	23	[001]	100
V	58	225	65	0	48	[001]	225
Mn	5	10	15	0	20	[001]	20
Co	35	10	8	0	33	[001]	35
Ni	180	123	130	0	178	[001]	180
Zr	773	778	290	0	788	[001]	788
Ru	175	623	113	0	490	[001]	623
Rh	820	95	323	0	815	[001]	820
Pd	213	15	0	218	198	[110]	218
Re	0	90	128	168	110	[100]	168
Os	150	150	0	333	183	[110]	333
Ir	158	0	333	140	145	[010]	333
Pt	1135	865	553	0	138	[001]	1135

Table S8 Exchange energies E_{ex} ($E_{ex} = E_{AFM} - E_{FM}$, meV) and parameters ($J_i$, meV) per supercell, average magnetic moment M (μ_B) per TM atom, and Curie/Néel temperatures (T_C/T_N, K) under biaxial strains from –10% (–14%) to 10% for Co_2@, Zr_2@, Mn_2@, and V_2@g-C_4N_3 monolayers.

Co_2@g-C_4N_3	–10%	–8%	–6%	–4%	–2%	0	2%	4%	6%	8%	10%
FM	–251.96133	–253.94852	–255.23548	–256.20703	–256.98581	–257.28596	–256.97594	–256.08339	–254.66385	–252.77745	–250.49203
AFM1	–251.64044	–253.46765	–254.85276	–255.96702	–256.97741	–257.27785	–256.96762	–256.07545	–254.65514	–252.76721	–250.48060
AFM2	–251.66054	–253.53066	–254.92820	–256.03649	–256.92616	–257.23987	–256.94647	–256.07238	–254.66958	–252.79570	–250.51702
E_{AFM1}-E_{FM}	320.89	480.87	382.72	240.01	8.4	8.11	8.32	7.94	8.71	10.24	11.43
E_{AFM2}-E_{FM}	300.79	417.86	307.28	170.54	59.65	46.09	29.47	11.01	–5.73	–18.25	–24.99
M	1.791	1.796	1.802	1.812	1.824	1.844	1.867	1.875	1.894	1.923	1.951
J	J_1 = 6.062 J_2 = 5.347	J_1 = 10.597 J_2 = 8.142	J_1 = 8.877 J_2 = 5.954	J_1 = 5.957 J_2 = 3.282	J_1 = –0.816 J_2 = 1.136	J_1 = –0.561 J_2 = 0.866	J_1 = –0.236 J_2 = 0.542	J_1 = 0.087 J_2 = 0.197	J_1 = 0.403 J_2 = –0.100	J_1 = 0.655 J_2 = –0.309	J_1 = 0.786 J_2 = –0.410
T_C/T_N	208	305	236	142	9	8.5	8	6	7	16.5	21.5

Zr_2@g-C_4N_3	–14%	–12%	–10%	–8%	–6%	–4%	–2%	0	2%	4%	6%	8%	10%
FM	–250. 11052	–255. 82160	–258.57351	–261.27068	–263.26412	–264.68895	–265.52275	–265.78790	–265.52975	–264.80555	–263.68648	–262.340763	–260.93541
AFM1	–249. 58492	–255. 01236	–257.72345	–260.68366	–263.02174	–264.55353	–265.40282	–265.68864	–265.45534	–264.75545	–263.67832	–262.33571	–260.83445
AFM2	–250. 10165	–255. 81481	–258.56191	–261.25587	–263.24120	–264.65982	–265.49586	–265.76366	–265.50498	–264.77630	–263.52231	–262.271783	–260.96364
$E_{AFM1} - E_{FM}$	525.600	809.24	850.06	587.02	242.38	135.42	119.93	99.26	74.41	50.1	8.16	5.053	100.96
$E_{AFM2} - E_{FM}$	8.87	6.79	11.6	14.81	22.92	29.13	26.89	24.24	24.77	29.25	164.17	68.98	–28.23
M	0.336	0.346	0.358	0.371	0.389	0.403	0.414	0.419	0.424	0.435	0.442	0.445	0.447
J	J_1 = 544.168 J_2 = 4.631	J_1 = 892.243 J_2 = 3.759	J_1 = 823.418 J_2 = 5.657	J_1 = 526.383 J_2 = 6.725	J_1 = 190.753 J_2 = 9.467	J_1 = 93.018 J_2 = 11.210	J_1 = 77.660 J_2 = 9.806	J_1 = 60.589 J_2 = 8.427	J_1 = 40.973 J_2 = 8.181	J_1 = 22.393 J_2 = 9.232	J_1 = –46.247 J_2 = 51.352	J_1 = –20.959 J_2 = 24.557	J_1 = 73.629 J_2 = –9.031
T_C/T_N	100	245	205	135	75	54	49	41.5	34	28	10	5	8

V_2@g-C_4N_3	–10%	–8%	–6%	–4%	–2%	0	2%	4%	6%	8%	10%
FM	–258.63834	–260.51049	–262.71802	–264.33130	–265.32042	–265.65474	–265.31972	–264.33069	–262.73079	–260.74988	–258.33754
AFM1	–258.48512	–260.69137	–262.63669	–264.09302	–265.11713	–265.49611	–265.21029	–264.28558	–262.77152	–260.74545	–258.28633
AFM2	–258.61151	–260.68917	–262.83188	–264.40861	–265.37347	–265.69036	–265.34754	–264.36781	–262.83566	–260.83029	–258.36567
E_{AFM1}-E_{FM}	153.22	–180.88	81.33	238.28	203.29	158.63	109.43	45.11	–40.73	4.43	51.21
E_{AFM2}-E_{FM}	26.83	–178.68	–113.86	–77.31	–53.05	–35.62	–27.82	–37.12	–104.87	–80.41	–28.13
M	2.717	2.746	2.766	2.836	2.952	2.952	2.968	2.975	2.981	2.986	2.99
J	J_1 = 2.318 J_2 = 0.222	J_1 = –1.313 J_2 = –1.282	J_1 = 1.953 J_2 = –0.804	J_1 = 3.883 J_2 = –0.542	J_1 = 3.213 J_2 = –0.371	J_1 = 2.482 J_2 = –0.251	J_1 = 1.750 J_2 = –0.197	J_1 = 0.913 J_2 = –0.266	J_1 = 0.182 J_2 = –0.815	J_1 = 0.729 J_2 = –0.657	J_1 = 1.105 J_2 = –0.238
T_C/T_N	9	< 5	< 5	18.5	16	13	9	< 5	< 5	< 5	< 5

Mn_2@g-C_4N_3	–10%	–8%	–6%	–4%	–2%	0	2%	4%	6%	8%	10%
FM	–260.23556	–263.34844	–265.76293	–267.49225	–268.53199	–268.88016	–268.53572	–267.52249	–265.89266	–263.72717	–261.12919
AFM1	–260.45080	–263.51882	–265.90249	–267.59159	–268.58463	–268.89152	–268.52121	–267.49765	–265.87130	–263.72309	–261.15011
AFM2	–260.33062	–263.44773	–265.86508	–267.58480	–268.61087	–268.94808	–268.59936	–267.58277	–265.94491	–263.76152	–261.14104
E_{AFM1}-E_{FM}	–215.24	–170.38	–139.56	–99.34	–52.64	–11.36	14.51	24.84	21.36	4.08	–20.92
E_{AFM2}-E_{FM}	–95.06	–99.29	–102.15	–92.55	–78.88	–67.92	–63.64	–60.28	–52.25	–34.35	–11.85
M	4.604	4.63	4.648	4.663	4.678	4.691	4.706	4.723	4.742	4.761	4.769
J	J_1 = –0.922 J_2 = –0.261	J_1 = –0.666 J_2 = –0.274	J_1 = –0.492 J_2 = –0.284	J_1 = –0.297 J_2 = –0.259	J_1 = –0.075 J_2 = –0.223	J_1 = 0.128 J_2 = –0.193	J_1 = 0.265 J_2 = –0.182	J_1 = 0.316 J_2 = –0.173	J_1 = 0.275 J_2 = –0.151	J_1 = 0.124 J_2 = –0.100	J_1 = –0.088 J_2 = –0.035
T_N	< 5	< 5	< 5	< 5	24	49	49	50.5	44	25	24

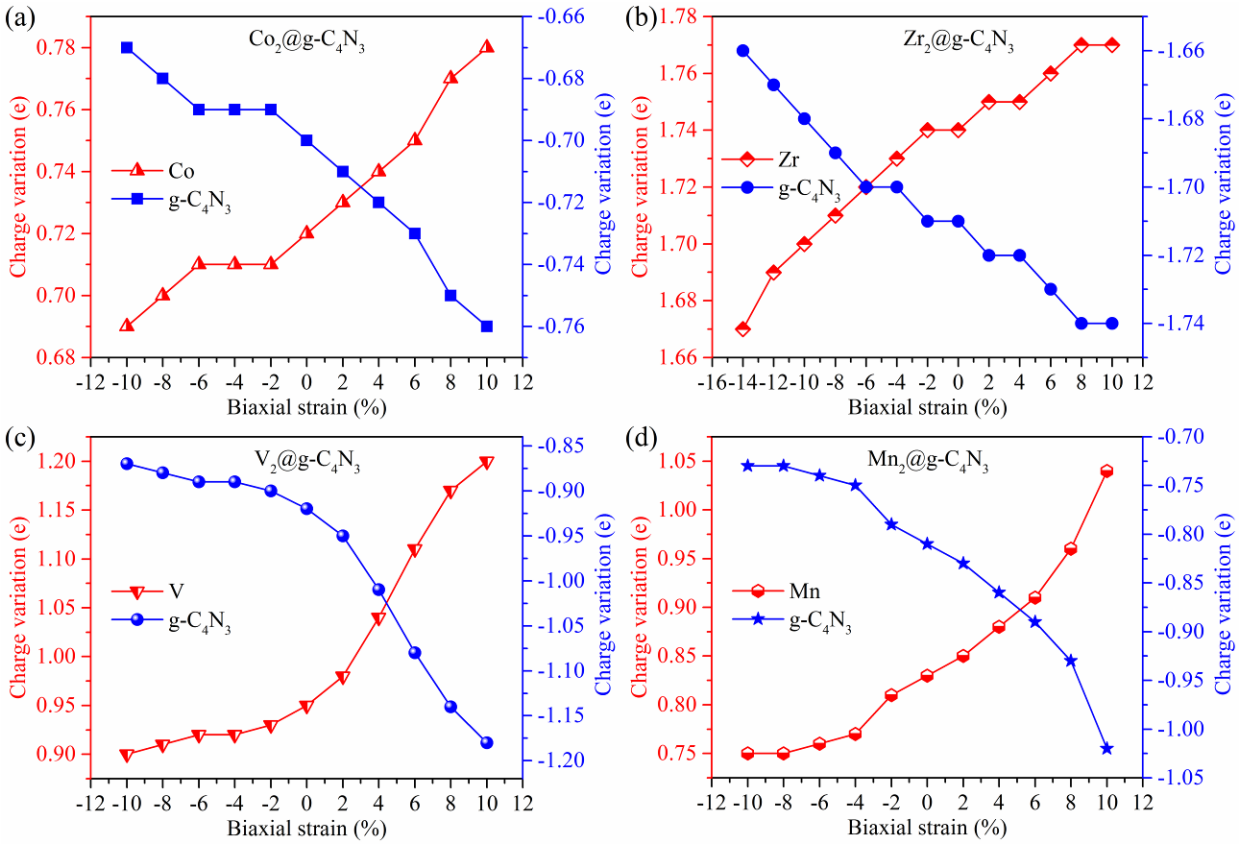

Fig. 15 (a)–(d) are the evolutions of calculated Bader charges on TM atoms and g-C_4N_3 moiety of four representative materials versus biaxial strains from –10% (–14%) to 10%.

(5) Electronic properties

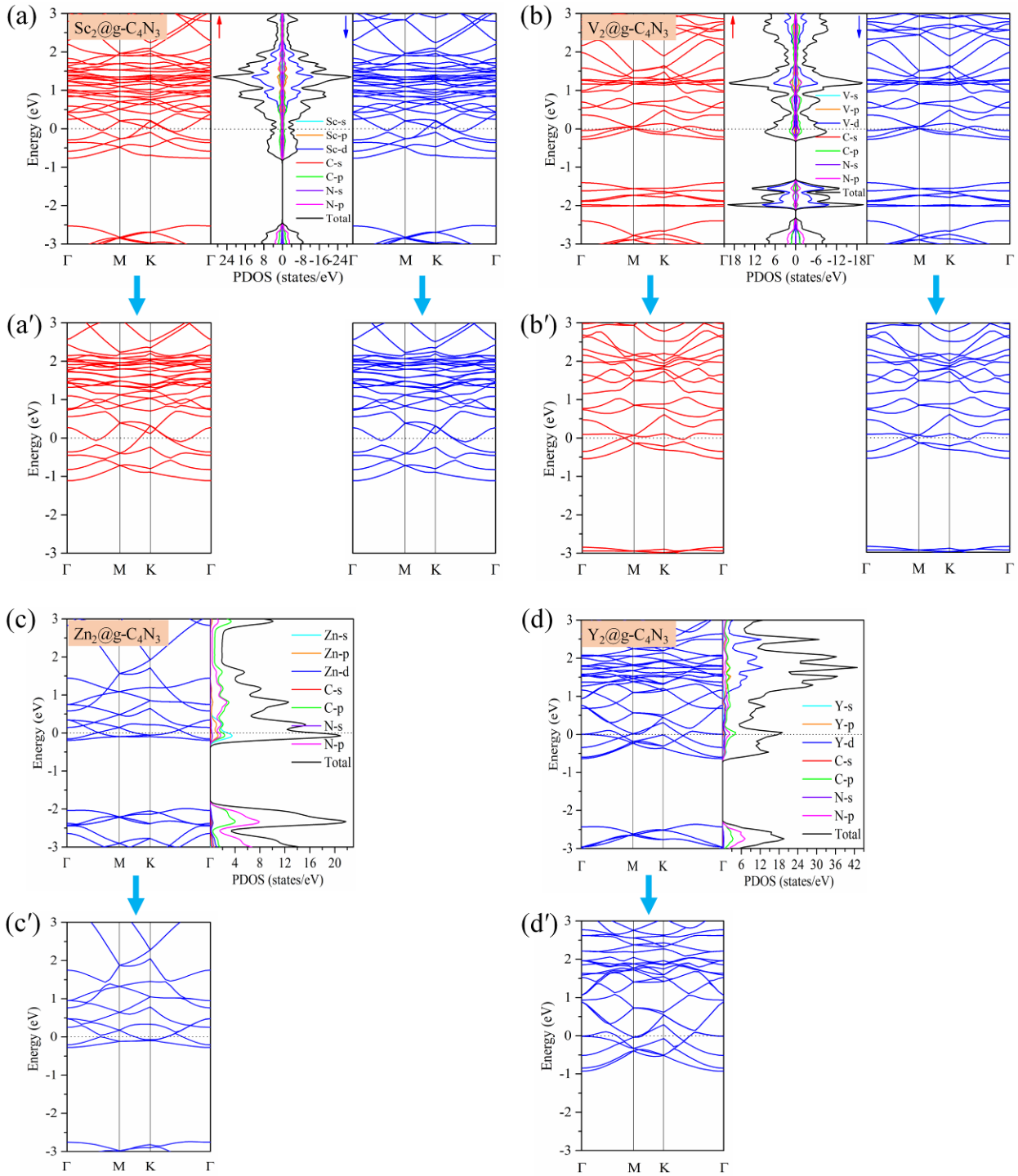

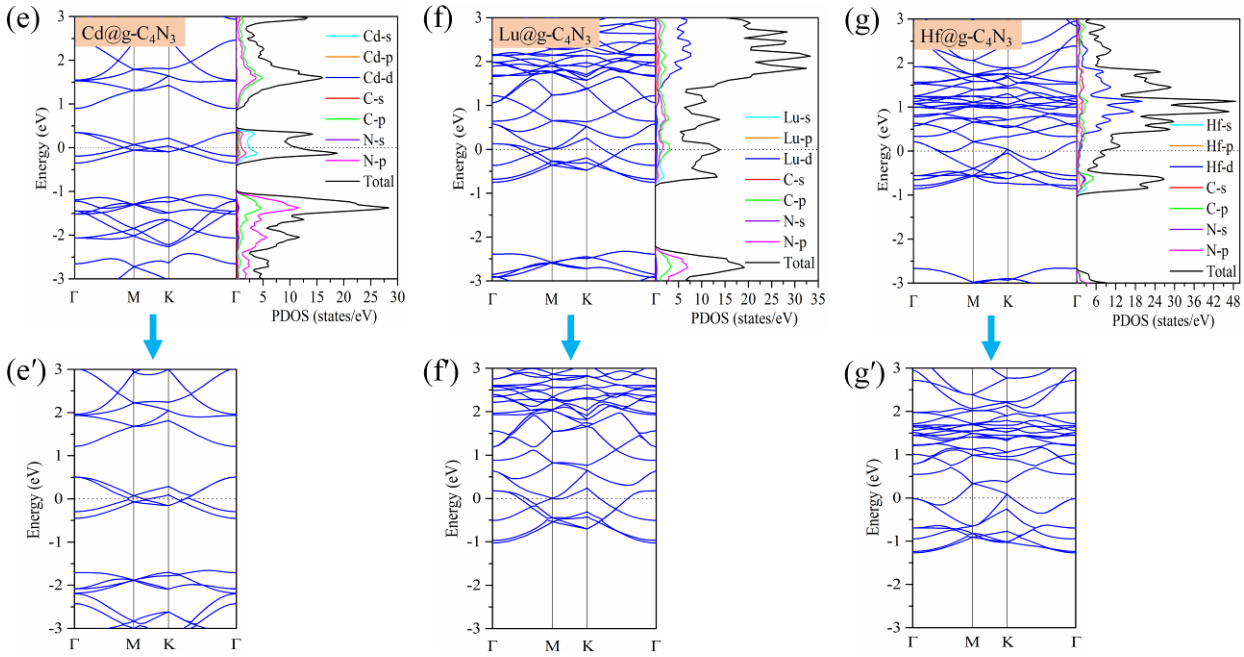

Figue S16 The band structures and PDOS for (a) Sc_2@, (b) V_2@, (c) Zn_2@, (d) Y_2@, (e) Cd_2@, (f) Lu_2@ and (g) Hf_2@g-C_4N_3 monolayers calculated at PBE+U level. (a′)–(g′) are band structures calculated at HSE06 level. Γ (0, 0, 0), M (0, 1/2, 0), and K (–1/3, 2/3, 0) are high symmetry points in the first Brillouin zone in reciprocal space. The PDOS of TM-*s*, TM-*p*, TM-*d*, C-*s*, C-*p*, N-*s*, N-*p*, and TDOS are plotted in light blue, orange, blue, red, green, violet, magenta, and black, respectively.

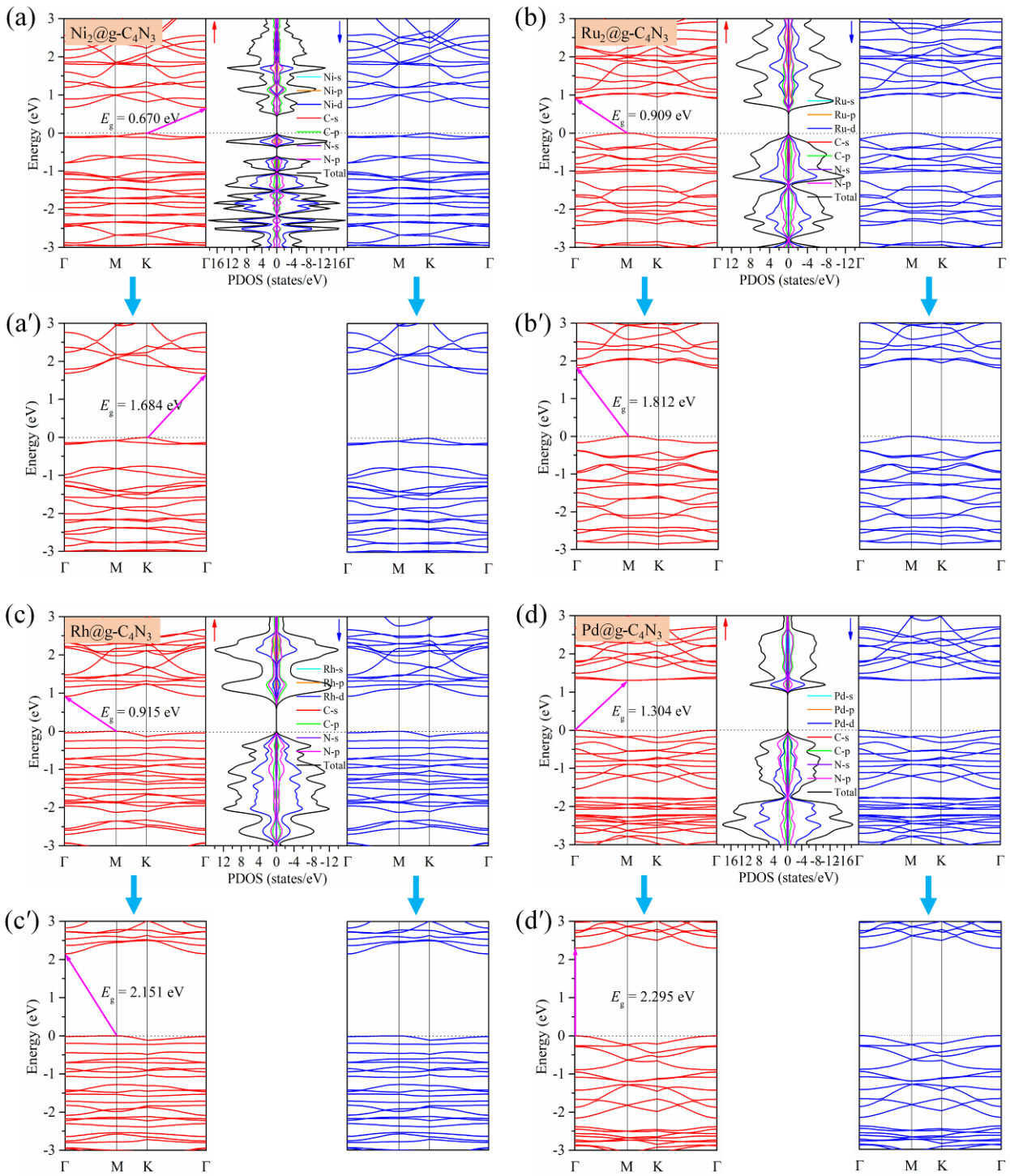
(a)
Ni2@g-C4N3
Eg = 0.670 eV
Ni-s
Ni-p
Ni-d
C-s
C-p
N-s
N-p
Total
(b)
Ru2@g-C4N3
Eg = 0.909 eV
Ru-s
Ru-p
Ru-d
C-s
C-p
N-s
N-p
Total
(a′)
Eg = 1.684 eV
(b′)
Eg = 1.812 eV
(c)
Rh@g-C4N3
Eg = 0.915 eV
Rh-s
Rh-p
Rh-d
C-s
C-p
N-s
N-p
Total
(d)
Pd@g-C4N3
Eg = 1.304 eV
Pd-s
Pd-p
Pd-d
C-s
C-p
N-s
N-p
Total
(c′)
Eg = 2.151 eV
(d′)
Eg = 2.295 eV
Energy (eV)
PDOS (states/eV)
Γ M K Γ

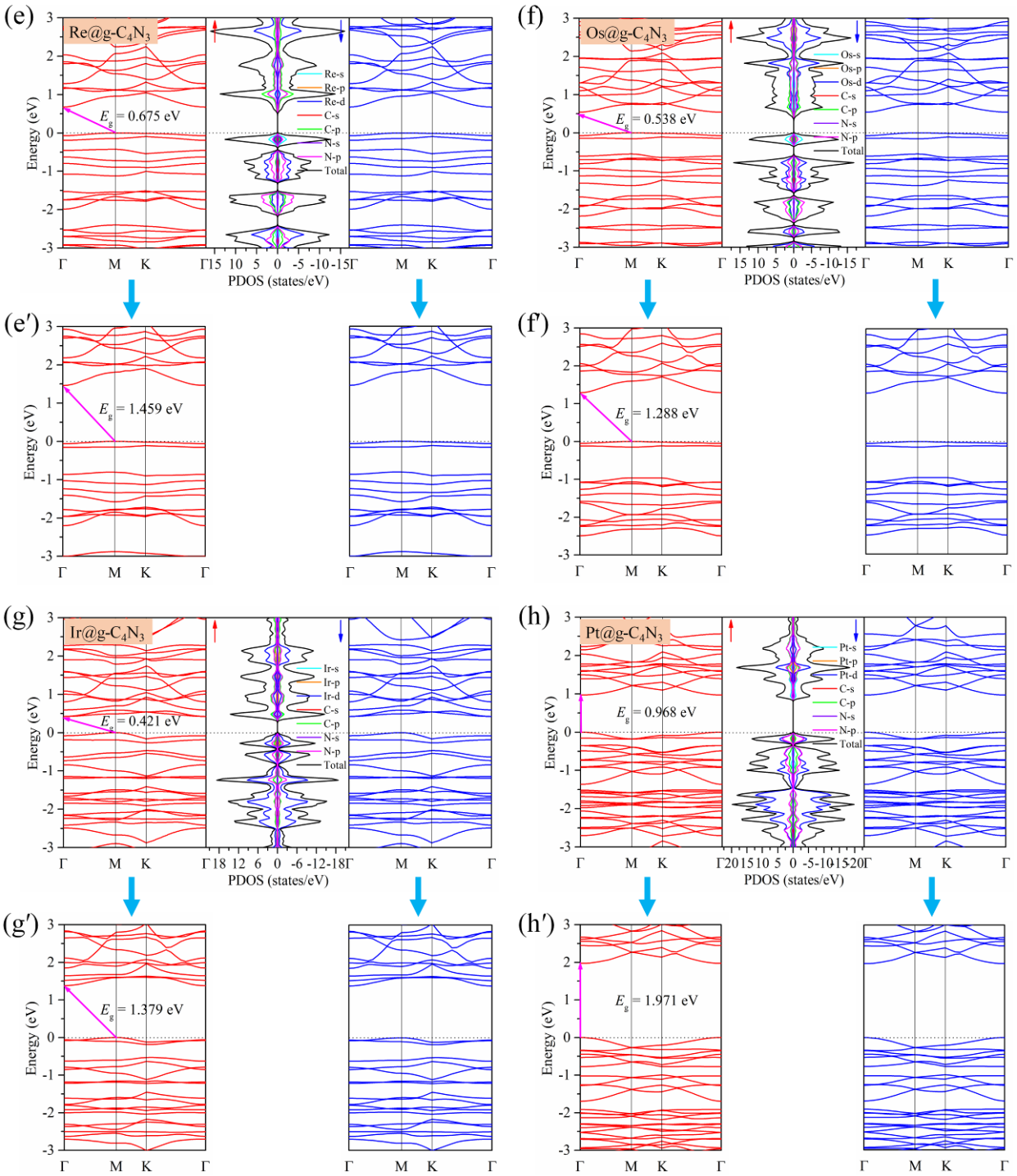

Fig. S17 The band structures and PDOS for (a) Ni_2@, (b) Ru_2@, (c) Rh_2@, (d) Pd_2@, (e) Re_2@, (f) Os_2@, (g) Ir_2@ and (h) Pt_2@g-C_4N_3 monolayers calculated at PBE+U level. (a′)–(h′) are band structures calculated at HSE06 level. Γ (0, 0, 0), M (0, 1/2, 0), and K (–1/3, 2/3, 0) are high symmetry points in the first Brillouin zone in reciprocal space. The PDOS of TM-*s*, TM-*p*, TM-*d*, C-*s*, C-*p*, N-*s*, N-*p*, and TDOS are plotted in light blue, orange, blue, red, green, violet, magenta, and black, respectively.

Table S9 Band gap values (eV) of pristine g-C_4N_3 and TM_2@g-C_4N_3 monolayers calculated at PBE+U and HSE06 levels, and the difference ΔE (eV) between the band gaps calculated at the two levels.

Structures	Magnetic	PBE+U	HSE06	ΔE
g-C_4N_3	FM	Spin up: 2.208 Spin down: 0	Spin up: 3.107 Spin down: 0	Spin up: 0.899 Spin down: 0
Sc_2@g-C_4N_3	AFM2	0	0	0
V_2@ g-C_4N_3	AFM2	0	0	0
Mn_2@g-C_4N_3	AFM2	0	0	0
Co_2@g-C_4N_3	FM	Spin up: 0.668 Spin down: 0.338	Spin up: 1.864 Spin down: 1.408	Spin up: 1.196 Spin down: 1.070
Ni_2@g-C_4N_3	AFM2	0.670	1.684	1.014
Zn_2@g-C_4N_3	NM	0	0	0
Y_2@g-C_4N_3	NM	0	0	0
Zr_2@g-C_4N_3	FM	Spin up: 0 Spin down: 0.967	Spin up: 0 Spin down: 1.505	Spin up: 0 Spin down: 0.538
Ru_2@g-C_4N_3	AFM1	0.909	1.812	0.903
Rh_2@g-C_4N_3	AFM1	0.915	2.151	1.236
Pd_2@g-C_4N_3	AFM2	1.304	2.295	0.991
Cd_2@g-C_4N_3	NM	0	0	0
Lu_2@g-C_4N_3	NM	0	0	0
Hf_2@g-C_4N_3	NM	0	0	0
Re_2@g-C_4N_3	AFM1	0.675	1.459	0.784
Os_2@g-C_4N_3	AFM1	0.538	1.288	0.750
Ir_2@g-C_4N_3	AFM1	0.421	1.379	0.958
Pt_2@g-C_4N_3	AFM1	0.968	1.971	1.003

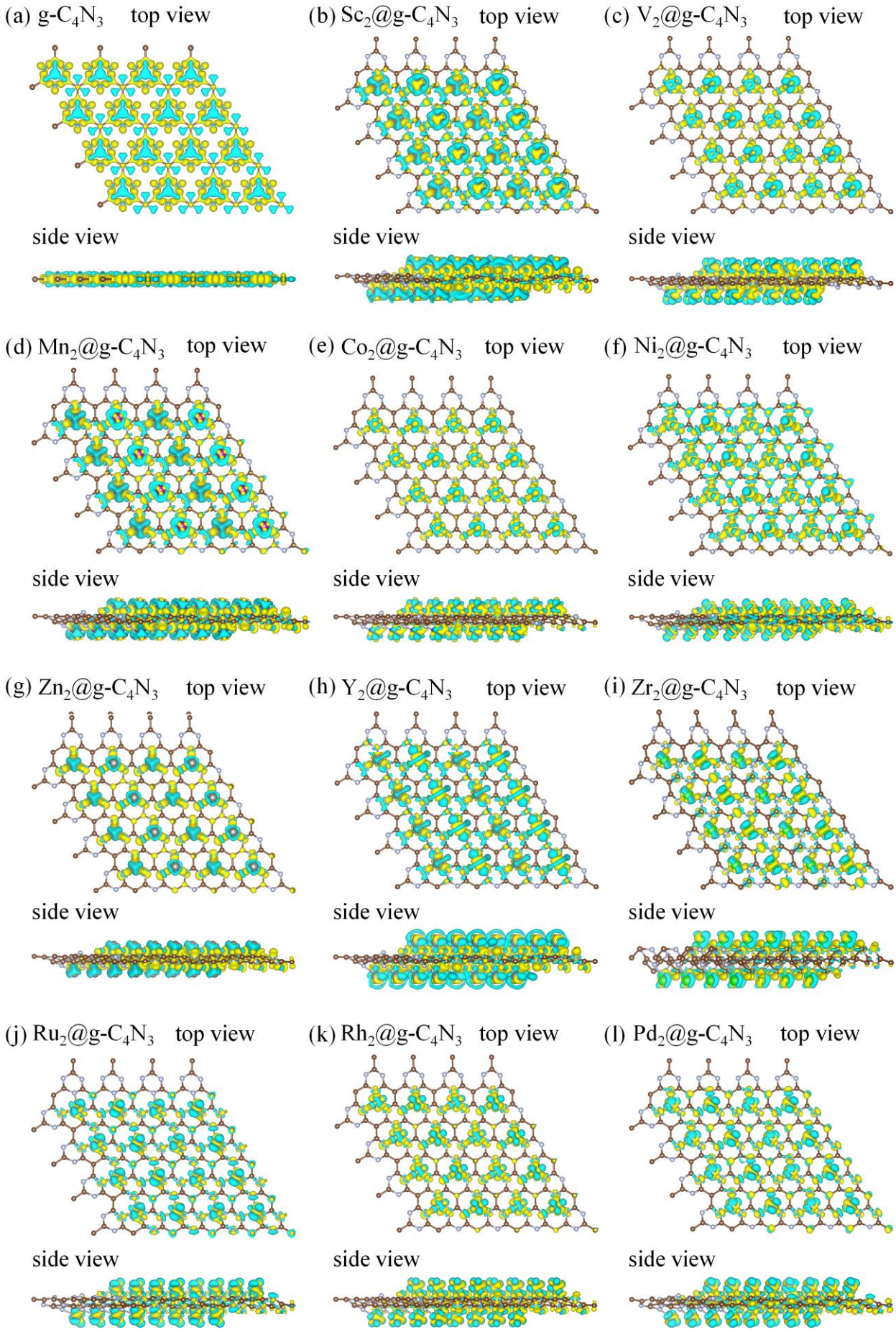
(a) g-C_4N_3 top view
side view
(b) Sc_2@g-C_4N_3 top view
side view
(c) V_2@g-C_4N_3 top view
side view
(d) Mn_2@g-C_4N_3 top view
side view
(e) Co_2@g-C_4N_3 top view
side view
(f) Ni_2@g-C_4N_3 top view
side view
(g) Zn_2@g-C_4N_3 top view
side view
(h) Y_2@g-C_4N_3 top view
side view
(i) Zr_2@g-C_4N_3 top view
side view
(j) Ru_2@g-C_4N_3 top view
side view
(k) Rh_2@g-C_4N_3 top view
side view
(l) Pd_2@g-C_4N_3 top view
side view

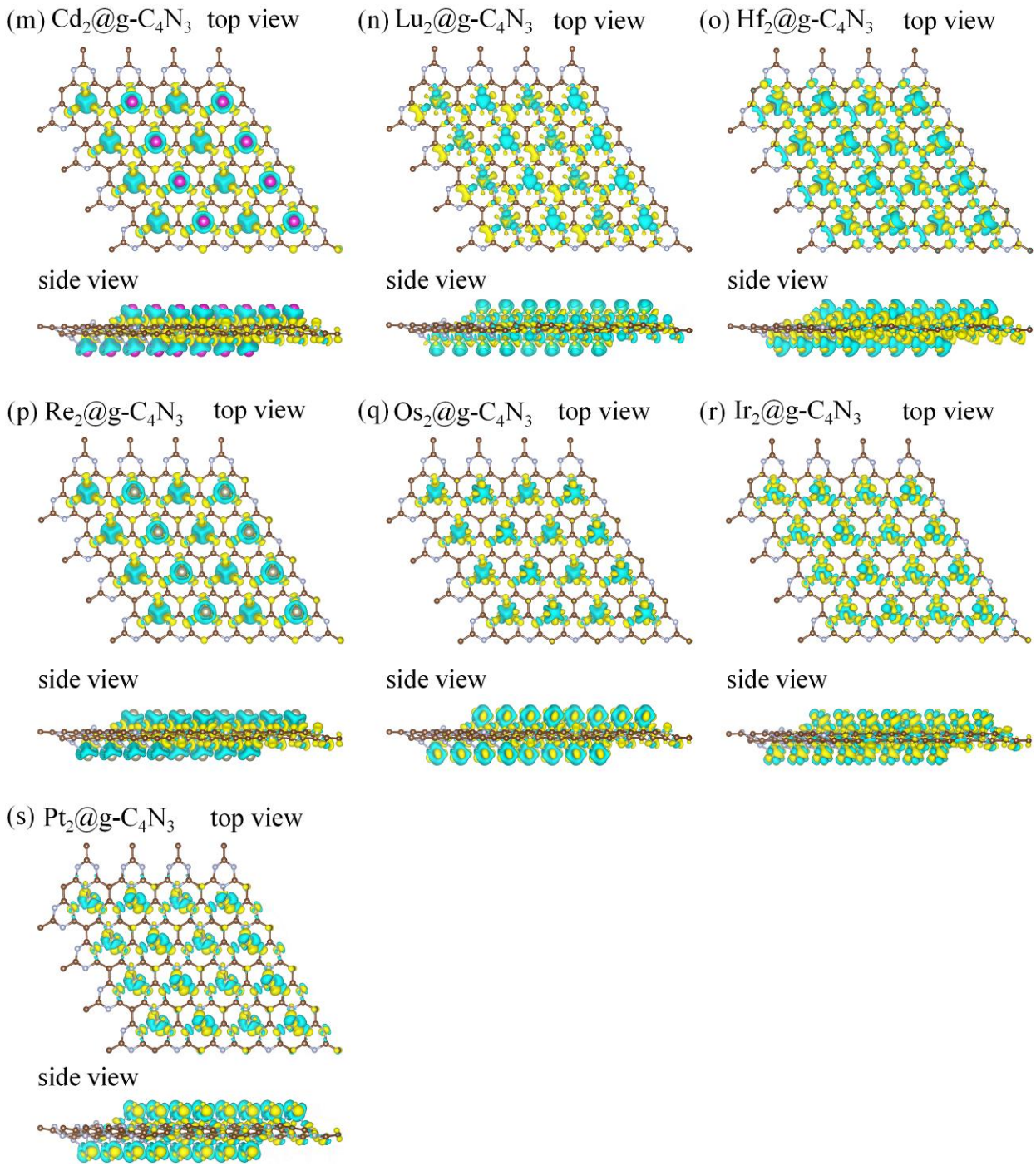

Fig. S18 Top and side views of the charge density difference for 2D periodic (a) g-C_4N_3, (b) Sc_2@, (c) V_2@, (d) Mn_2@, (e) Co_2@, (f) Ni_2@, (g) Zn_2@, (h) Y_2@, (i) Zr_2@, (j) Ru_2@, (k) Rh_2@, (l) Pd_2@, (m) Cd_2@, (n) Lu_2@, (o) Hf_2@, and (p) Re_2@, (q) Os_2@, (r) Ir_2@, and (s) Pt_2@g-C_4N_3 monolayers in $2 \times 2 \times 1$ supercells at an isosurface value of 0.01 e $Å^{-3}$. Yellow and blue bubbles represent charge accumulation and depletion, respectively.

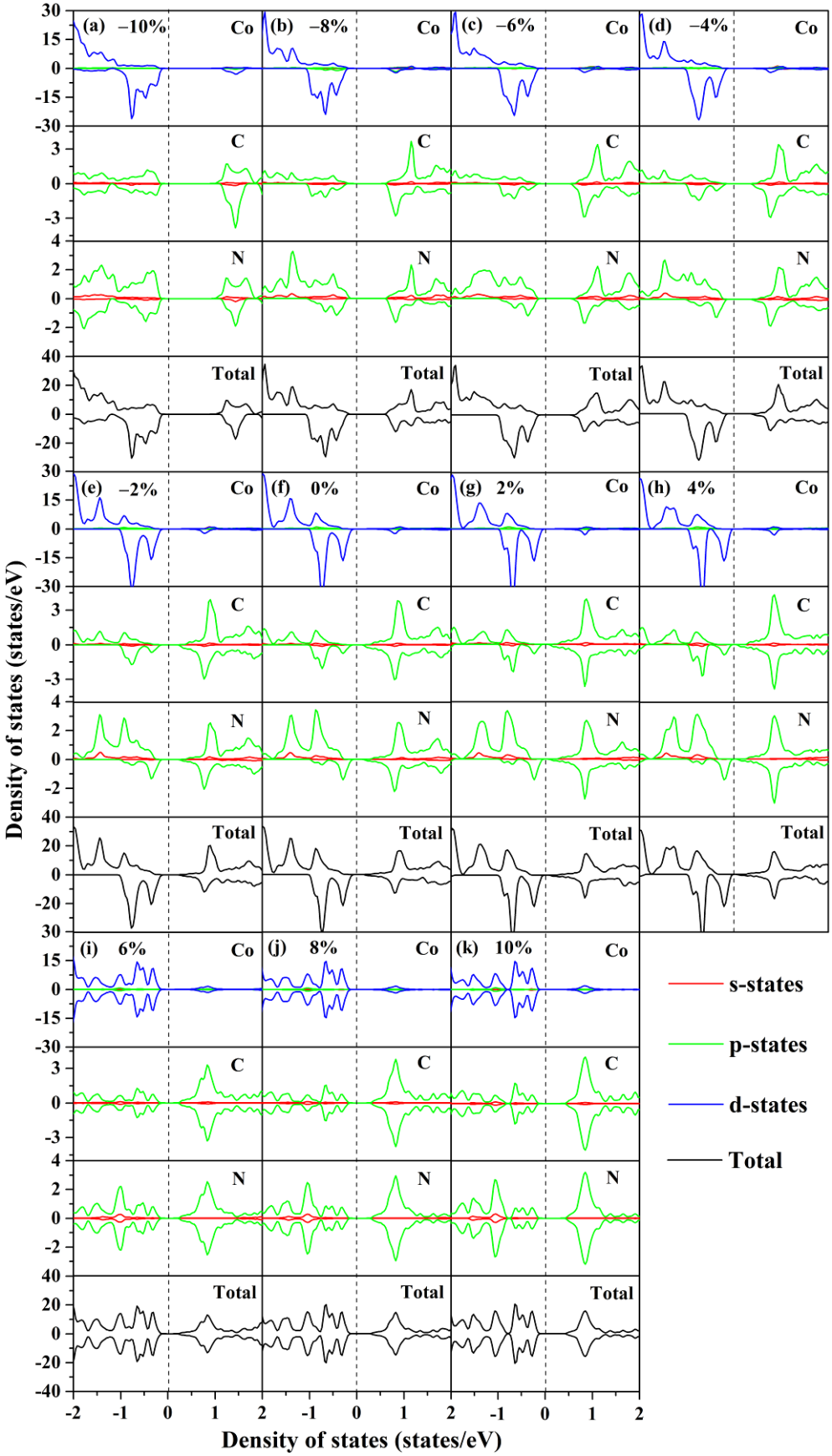

Fig. S19 The evolution of PDOS of different atoms near the Fermi level versus biaxial strains from –10% to 10% for Co_2@g-C_4N_3 monolayer. The Fermi level has been set to 0 eV.

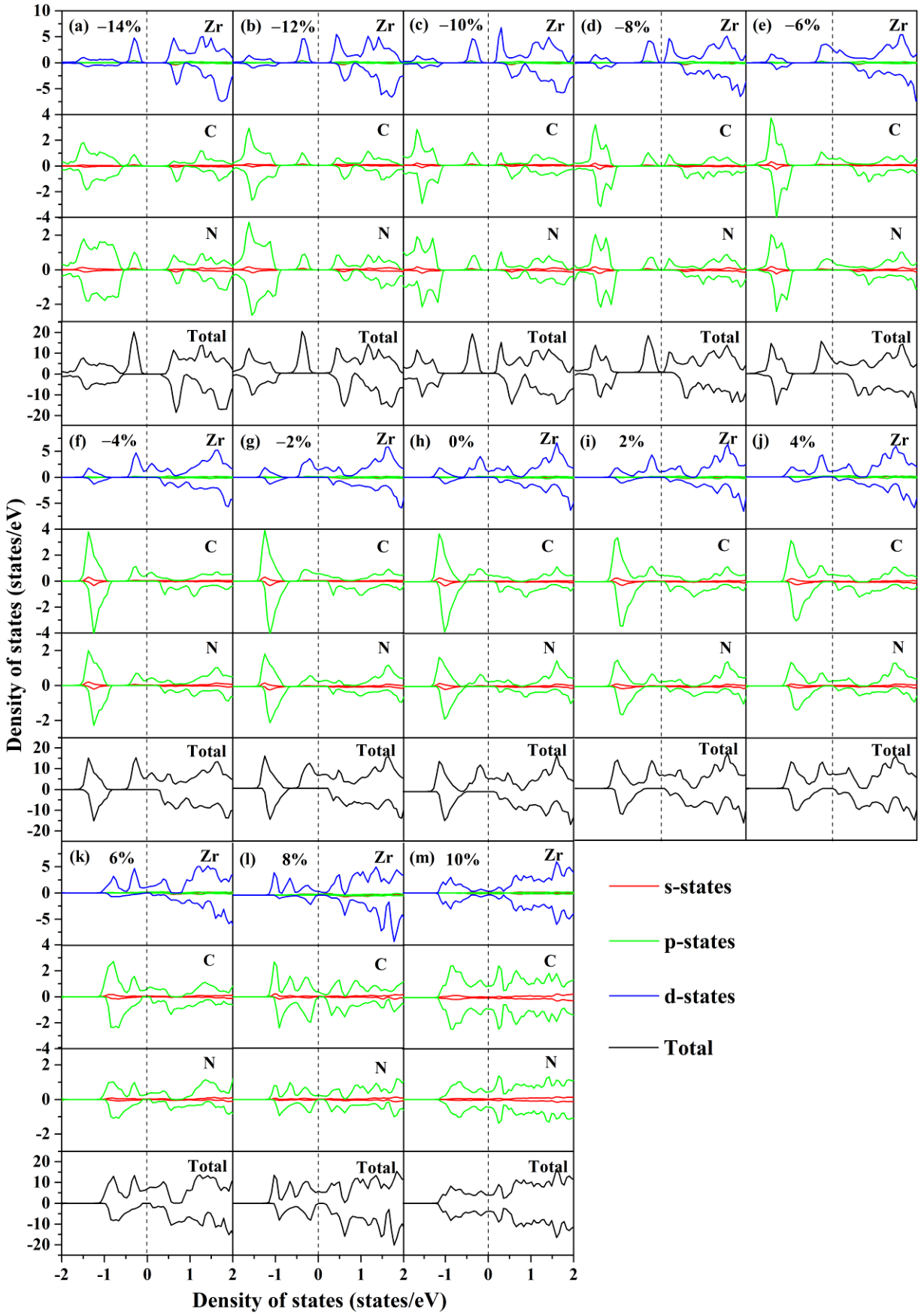

Fig. S20 The evolution of PDOS of different atoms near the Fermi level versus biaxial strains from –14% to 10% for Zr_2@g-C_4N_3 monolayer. The Fermi level has been set to 0 eV.

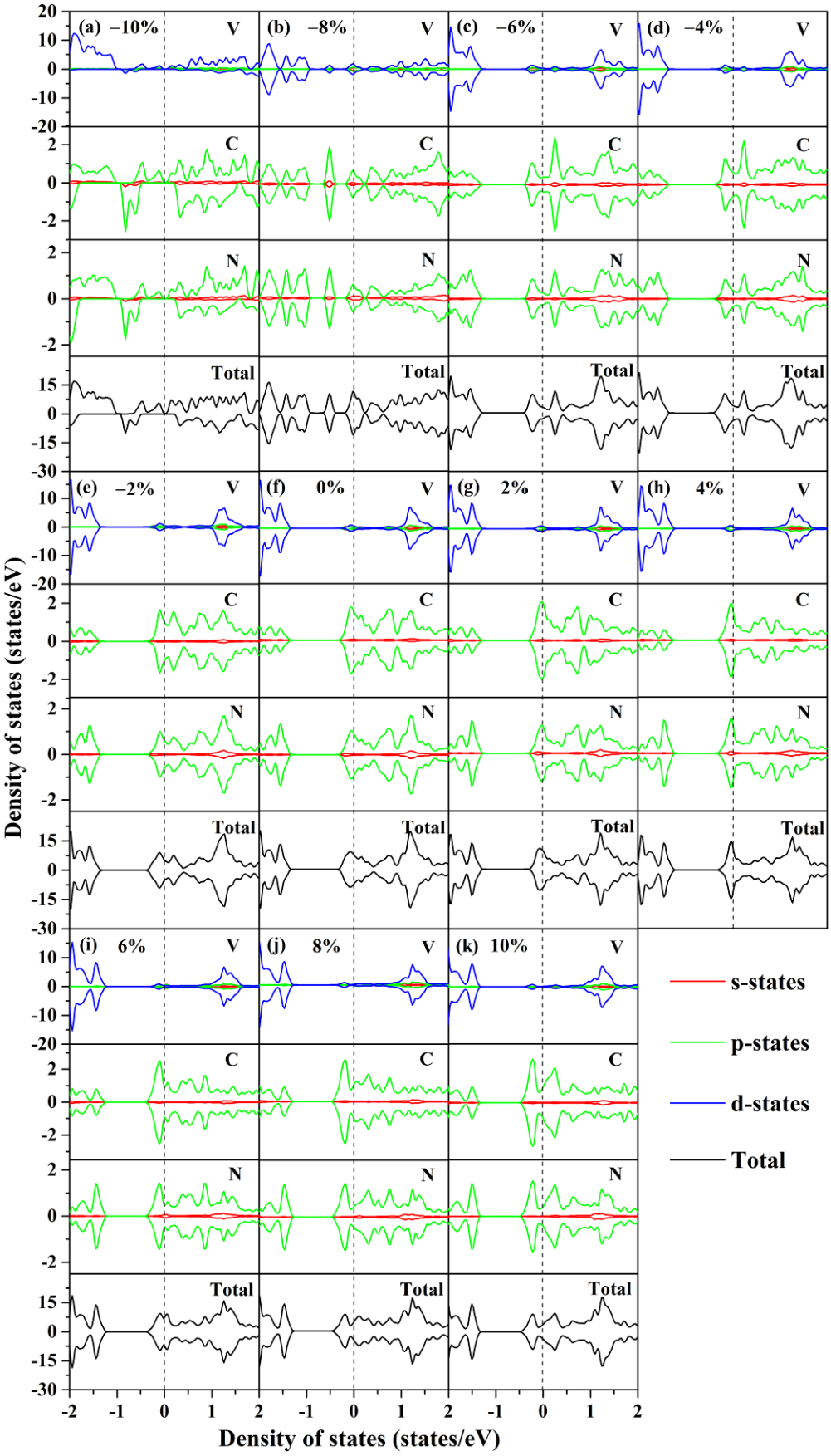

Fig. S21 The evolution of PDOS of different atoms near the Fermi level versus biaxial strains from –10% to 10% for V_2@g-C_4N_3 monolayer. The Fermi level has been set to 0 eV.

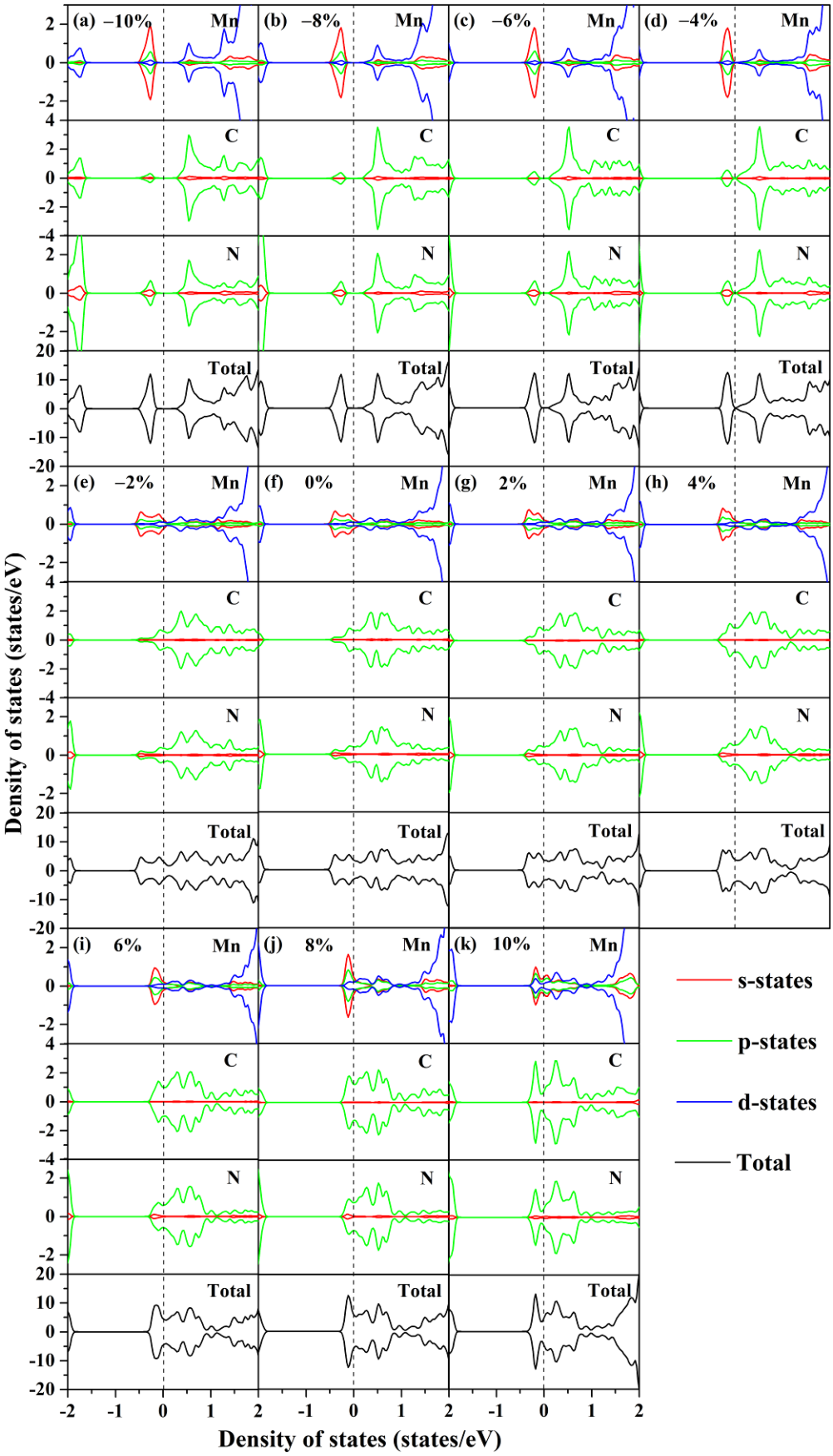

Fig. S22 The evolution of PDOS of different atoms near the Fermi level versus biaxial strains from –10% to 10% for Mn_2@g-C_4N_3 monolayer. The Fermi level has been set to 0 eV.

(6) Optical properties

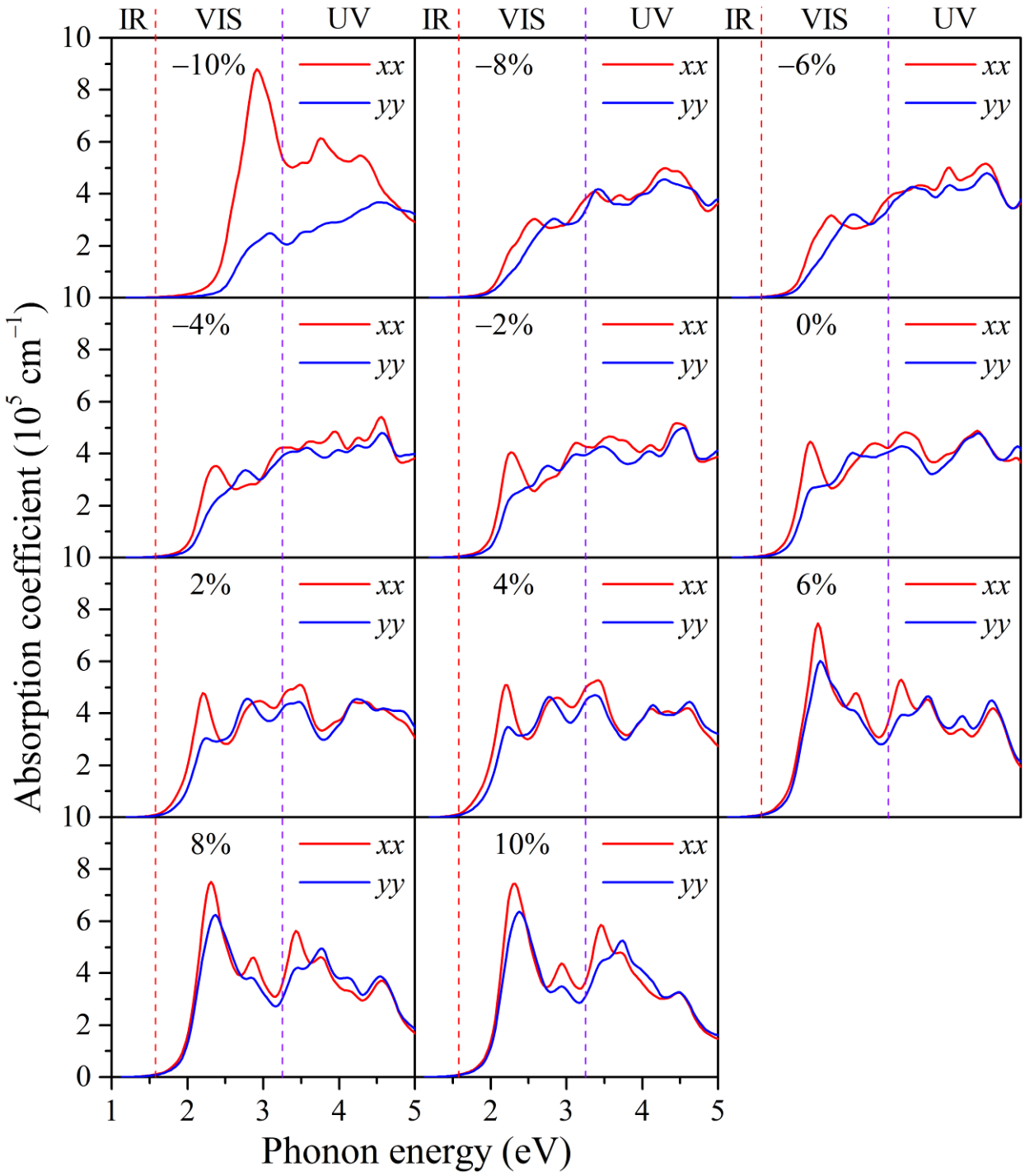

Fig. S23 The evolution of optical absorption coefficient versus biaxial strains from –10% to 10% for Co_2@g-C_4N_3 monolayers. The infrared, visible and ultraviolet regions are marked by red and purple dashed lines.

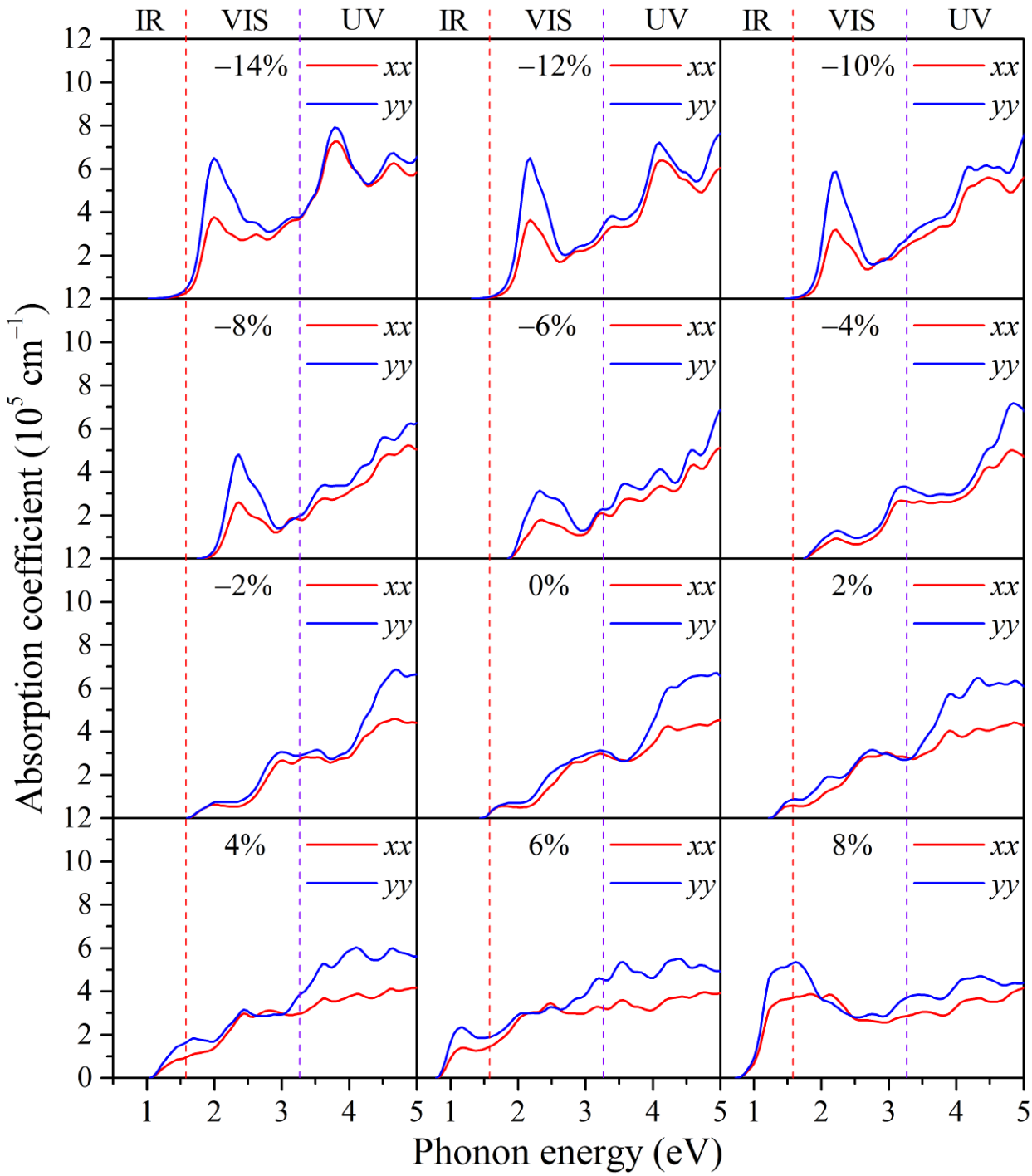

Fig. S24 The evolution of optical absorption coefficient versus biaxial strains from –14% to 8% for Zr_2@g-C_4N_3 monolayers. The infrared, visible and ultraviolet regions are marked by red and purple dashed lines.